REPORT DOCUMENTATION PAGE

Public reporting burden for this collection of information is estimated to everage 1 hour per response, including the time for reviewing instructions, searching existing data sources, gathering
deta needed, and completing and reviewing this collection of information. Send comments regarding this burden estimate or eny other espect of this collection of information, including suggestions for reducing
this burden to Depertment of Defense, Washington Headquarters Services, Diractorate for Information Operations and Reports (0704-0188), 1215 Jefferson Davis Highway, Suite 1204, Arlington, VA 22202-
4302. Respondents should be aware that notwithstanding any othar provision of law, no person shall be subject to any penalty for failing to comply with a collection of information if it does not display a currently
velid OMB control number. **PLEASE DO NOT RETURN YOUR FORM TO THE ABOVE ADDRESS.**

1. REPORT DATE (DD-MM-YYYY) 03-02-2009	2. REPORT TYPE Final		3. DATES COVERED (From - To) April 1,2005 – Aug 31,2008
4. TITLE AND SUBTITLE			5a. CONTRACT NUMBER FA 9550-05-1-0196
			5b. GRANT NUMBER
			5c. PROGRAM ELEMENT NUMBER
6. AUTHOR(S) Minoru Taya, Onur C. Namli and Tucker Howie			5d. PROJECT NUMBER
			5e. TASK NUMBER
			5f. WORK UNIT NUMBER
7. PERFORMING ORGANIZATION NAME(S) AND ADDRESS(ES) Department of Mechanical Engineering, CIMS, University of Washington, Box 352600 Seattle, WA 98195-2600			8. PERFORMING ORGANIZATION REPORT NUMBER CIMS-01-2009
9. SPONSORING / MONITORING AGENCY NAME(S) AND ADDRESS(ES) Air Force Office of Scientific Research *875 N. Randolph Street, Suite 325 Room* Arlington, VA 22203 ATTN: Dr Les Lec, Program Manager			10. SPONSOR/MONITOR'S ACRONYM(S) AFOSR
			11. SPONSOR/MONITOR'S REPORT NUMBER(S)

12. DISTRIBUTION / AVAILABILITY STATEMENT
unlimited

20090723670

13. SUPPLEMENTARY NOTES

14. ABSTRACT

   This AFOSR core program on Active composites is aimed to study analytically and experimentally new types of active composites, ferromagnetic shape memory alloy(FSMA) composite, shape memory alloy(SMA) fiber/shape memory polymer(SMP) composite, and piezoelectrics-SMA composite. The mechanism behind these new active composites is synergistic effects among these active materials, under various stimuli conditions. Airborn applications of these active composites are clearly stated in the report, ranging from synthetic jet actuator, superconfigurable structures and energy harvesting device under fluctuating high temperatures.

15. SUBJECT TERMS

16. SECURITY CLASSIFICATION OF:			17. LIMITATION OF ABSTRACT	18. NUMBER OF PAGES	19a. NAME OF RESPONSIBLE PERSON
a. REPORT	b. ABSTRACT	c. THIS PAGE			19b. TELEPHONE NUMBER (include area code)

Standard Form 298 (Rev. 8-98)
Prescribed by ANSI Std. Z39.18

AIR FORCE OFFICE OF SCIENTIFIC RESEARCH

DTIC Data

Purchase Request Number:	FQ8671-0500850
BPN:	F1ATA05024B850
Proposal Number:	04-NA-207
Research Title:	DESIGN OF ACTIVE COMPOSITES
Type Submission:	~~New Work Effort~~ Final Report
Inst. Control Number:	FA9550-05-1-0196DEF
Institution:	UNIVERSITY OF WASHINGTON
Primary Investigator:	Professor Minoru Taya
Invention Ind:	none
Project/Task:	2302B / X
Program Manager:	Byung-Lip Lee

Objective:

To develop the science base necessary to design and manufacture new "active"composite systems which allow high actuation speed as well as high force and large stroke capability of compact airborne actuators for smart structures; (for additional funding) to develop "self-strengthening" composites based on active materials.

Approach:

Relying on experience established under the current AFOSR-sponsored program on "ferromagetic shape memory alloy composites," the second phase of the research will focus on the design and manufacturing of new active composites based on various combinations of piezo-ceramics (PMN-PT, PZT), shape memory alloy (TiNi, CuAlMn), ferromagetic shape memory alloy (NiAlCo, FePd, NiMnGa) and/or thermoelectric materials. A new processing route of Spark Plama Sintering, awarded as a DURIP project, will be used to create particulate composites composed of shape memory alloy and ferromagnetic materials. The microstructure of each active composites will be optimized by analtical modeling to achieve higher force and stroke of the resulting actuators and more efficient energy harvesting capability of the components. (For additional funding) In collaboration with a research team at Hokkaido Univ., self-strengthening composites will be designed by incorporating nanofibers of shape mememory alloys or shape memory poymers and inducing compressive stress in the matrix region through shape or length change of shape memory nanofibers.

Progress:

Year: 2006   **Month:** 03

Annual Report:

Active materials in general and Ferromagnetic Shape Memory Alloy (FSMA) composites in particular have attracted a strong interest among many researchers in recent years as possible material for use in fast responsive actuators. Earlier works on FSMAs focusing on phase transformation under change in temperature of Fe-Pd system [1] and Ni-Mn-Ga systems [2] have been well documented in the past. In principal, there are three existing actuation modes associated with FSMAs using magnetic field as the driving force for actuation [3-7], namely: (i) magnetic field-induced phase transformation, (ii) martensite variant rearrangement and (iii) hybrid mechanism.

Year: 2007   **Month:** 12

Annual Report: 01 Seep 2005 - 01 Sep 2006

This annual report covers the progress in the active composites, two designs, (i) Ferromagnetic shape memory alloy(FSMA) composites and (ii) SMA-piezo composites. The former design is cost-effective route of designing and processing of ferromagnetic shape memory alloys by using two constitutive materials, ferromagnetic material and SMA of

Progress:

Year: 2007   **Month:** 12

super elastic grade. This FSMA composite is for use as a new airborne actuator. This report focuses both on modeling and processing. This report also states the design of a new active composite, SMA-piezo composite, which will be used as a new actuator material and also thermal energy harvester.

Year: 2008   **Month:** 01

Annual Report: 02 Sep 2006 - 31 Dec 2007

This annual report covers the progress in the active composites, two designs, (i) SMA-piezo composites, and (ii) shape memory alloy/shame memory polymer composites. The former design is SMA-piezo composite, which will be used as a new actuator material and also thermal energy harvester, while the latter is new design of active composite with large shape change for possible use in future morphing structures.

Year: 2008   **Month:** 10

We have progressed in deign and processing of particulate ferromagnetic SMA composites made of Fe and NiTi of super elastic grade, and the composite exhibited both ferromagnetic and super elastic behavior , these experimental data are predicted by a new analytical model based on Eshelby type. We also worked on piezoelectric films for detecting the loading history of structures, the results of which will be used for future structural health monitoring of airplane structures. Some preliminary results are obtained on shape memory polymers.

Year: 2009   **Month:** 06   **Final**

This AFOSR core program on Active composites is aimed to study analytically and experimentally new types of active composites, ferromagnetic shape memory alloy(FSMA) composite, shape memory alloy(SMA) fiber/shape memory polymer(SMP) composite, and piezoelectrics-SMA composite. The mechanism behind these new active composites is synergistic effects among these active materials, under various stimuli conditions. Airborn applications of these active composites are clearly stated in the report, ranging from synthetic jet actuator, superconfigurable structures and energy harvesting device under fluctuating high temperatures.

Final Report to AFOSR Grant (FA9550-05-1-0196)

Design of Active Composites

by
Minoru Taya, Director
Boeing-Pennell Professor
Center for Intelligent Materials and Systems
Department of Mechanical Engineering
University of Washington, Box 352600
Seattle, WA 98195-2600
Phone: 206-685-2850, Fax: 206-685-8047
Email: tayam@u.washington.edu

March 30, 2009

Table of Contents

Chapter 1.   Introduction

Active composites are made of active material of one kind embedded in a matrix material which may be structural host material, or another kind of active material. In this final report, we shall report four different active composites: (i) ferromagnetic shape memory alloy which is composed of shape memory alloy (SMA) and ferromagnetic matrix, (ii) SMA and piezoelectric ceramics(SMA-piezo composite) for fast-responsive actuator, (iii) SMA-piezo composite for thermal energy harvester, and (iv) morphing material composed of nano-SMA fiber and shape memory polymer matrix. All four cases of active composites are potentially useful materials for airborne specific applications, the first two for fast-responsive actuators and the third for thermal energy harvester and the fourth for morphing structures.

All four active composites are based on micro-mechanics based modeling, (i) Eshelby type modeling and (ii) laminate modeling which the authors developed during this project. Except for the second active composite (SMA-piezo composite), all other three active composites involve processing and characterization studies, the results of which are compared with the analytical results predicted by the models ensuring the validity of the proposed design and modeling.

As a natural extension of active composites, we found that use of nano-sized fillers is effective in enhancement of the overall composite properties; however this is met with technical challenges, such as processing. This is particularly true for SMA nanofibers in processing of SMA nanofibers/shape memory polymer matrix composite which should be further studied in near future.

It is noted that the new concept of using SMA and piezoelectric phases was originally for fast-responsive actuator materials, however, later stage of this project, we found that use of SMA-piezo composite is also effective for use in a new thermal energy harvester where temperature is fluctuating.

Chapter 2.   Design of ferromagnetic shape memory alloy composite made of Fe and TiNi particles

Ferromagnetic Shape Memory Alloy (FSMA) particulate composites have been processed by spark plasma sintering with varying weight fractions of NiTi (51 at% Ni) and Fe powders. An assortment of experimental processing conditions such as temperature, pressure, duration of sintering, heating rate has been chosen to characterize the relative density and superelasticity behavior of said FSMA composite. The effective magnetic properties of these processed composites have also been experimentally estimated using Vibration Sample Magnetometry (VSM). An attempt at predicting the effective magnetic properties of the FSMA composite based on Eshelby's inhomogeneous inclusion method in conjunction with Mori-Tanaka's mean field theory for larger concentrations of the ferromagnetic phase has also been presented in this study. The analytical model results thus obtained are compared with experimental data resulting in a reasonably good agreement.

2.1. Introduction

Ferromagnetic shape memory alloys (FSMAs) have attracted strong attention among material science community in particular as well as actuator designers at large mainly due to their fast-response and large strain capabilities. Popular FSMAs that have been extensively studied include NiMnGa (Ullakko 1997, James 1998, Murray 1998, Kakeshita 2000 and Liang 2001) and FePd (Kato 2002, Liang 2002, and Wada 2003) systems. There are three mechanisms of actuation associated with FSMAs, under magnetic field namely, (i) magnetic field-induced phase transformation, (ii) martensite variant rearrangement and (iii) hybrid mechanism (Liang 2006). The first two mechanisms are operative under constant magnetic field, while the third mechanism is based on gradient magnetic field.

An earlier study by Kato et al 2002 which was based on thermodynamics, made a preliminary estimate of the magnetic energy necessary to induce a phase transformation in FSMAs. The general conclusion was that large magnetic (H) field was required for the phase change to take for both NiMnGa and FePd systems. Therefore, the first mechanism was deemed unsuitable for use in designing compact actuators which may need a small and portable electromagnet system as a driving unit.

The second mechanism involves inducing the strain in a FSMA with 100% martensite phase and subjecting it to a *constant* H-field which acts on the magnetic moments in magnetic domains that exist in the martensite phase so as to rotate them along the easy axis, i.e., e-axis in the case of NiMnGa and FePd systems. Even though the strain induced by the second mechanism is very large, the corresponding stress remains as modest as several MPa under modest applied magnetic flux density (1 T). Thus, the use of the second mechanism may be advantageous to design an actuator with large strain capability.

The third mechanism (Kato 2002, Liang 2006) termed as 'hybrid mechanism' is based on a set of chain reactions. An applied magnetic flux (or field) *gradient* induces magnetic force which causes stress induced martensite phase transformation resulting in the phase change from stiff austenite to soft martensite phase thereby leading to large displacement. The advantages of this are large stress (100 MPa in the case of FePd), modest to intermediate strain and fast actuation time. Physically, such a phase change can be achieved by approaching a compact and portable magnet close to the FSMA specimen which provides a large magnetic field gradient. Therefore, the third

'hybrid' mechanism is considered most suited for use in designing compact actuators with large force capability.

However, the cost of processing FSMAs such as FePd is very expensive. On the other hand, superelastic shape memory alloys have high mechanical performances, large transformation strain and stress capabilities. However, the speed of superelastic SMAs by changing *temperature* is slow. If a ferromagnetic shape memory alloy composite composed of a ferromagnetic material (soft magnet) and a superelastic SMA can be developed and such a composite be actuated based on the hybrid mechanism, novel cost-effective and high-speed actuators can be designed. This has been the underlying motivation of the present work. In the design of such a composite, the requirements have been identified as: no plastic deformation of the ferromagnetic material and large transformation strain in superelastic SMA. In order to achieve the optimum microstructure of FSMA composites for actuator design, numerical models such as FEM, or an analytical approach need to be developed. Such as analytical model for FSMA composites with the aim of optimizing the microstructure of FSMA composite with emphasis on laminated composite and helical shaped composite has been developed earlier (Kusaka 2004).

This study reports the analytical modeling of magnetic properties of FSMA particulate composites, and also elucidates the experimental work of processing such composites. The validity of the proposed model has been established by comparison with measured magnetic properties of the composite.

This part of the study has been organized as follows: - the processing of particulate Fe-TiNi composite using Spark Plasma Sintering (SPS) with various concentrations of Fe will be discussed in section 2.2 followed by the analytical model for predicting the effective magnetic properties of the particulate composites in section 2.3, a brief discussion of the results and validity of the proposed model has been presented in section 2.4 followed by some conclusions in section 2.5.

2.2. Processing of Particulate Fe-TiNi Composite

The FSMA composite used in the present work is a "particulate composite" composed of particulate powders of SMA (TiNi) and ferromagnetic material (soft magnetic Fe). The ordinary metallurgical route for processing particulate composites using powders i.e., standard sintering produces unwanted reaction products destroying the original properties of constituent SMA and ferromagnet. In order to circumvent unwanted reaction byproducts, Spark Plasma Sintering (SPS) machine was used to process the particulate composites. The SPS machine has been recently installed at Center for Intelligent Materials and Systems, University of Washington, Seattle (Dr. Sinter SPS-515S, Sumitomo Coal Mining Co., Japan). Figure 2.1 is a schematic illustrating the working of the SPS equipment and the sintering process (SPS Syntex Inc Manual). It has been reported that sintering conducted using the SPS machine under high temperatures and pressure of around 25-50 MPa for as short a time as 5 minutes in near vacuum conditions (~5-6 Pa) followed by rapid cooling using Argon gas produces remarkably good results (Gururaja 2006). In fact, as shown earlier, due to the short sintering time, the samples produced at CIMS were of extremely high quality exhibiting low percentage of the intermetallics (Gururaja 2005).

In this study, two different kinds of TiNi powders have been used namely, (1) large Micro-sized TiNi (Ni 50.9at.% and Ti 49.1at.%) with average diameter of 212 μm supplied by Sumitomo Metals, Japan and (2) smaller Nano-sized TiNi (51at%Ni and 49at%Ti) with average diameter of 100 nm supplied by Argonide, USA. An ingot of TiNi alloy made by Sumitomo Metals, Osaka, Japan, was shipped to Fukuda Metals, Kyoto, Japan, where Plasma Rotating Electrode Process

(PREP) was used to process TiNi powders with average diameter of 212 µm. The particulate FSMA composite specimens obtained using these powders were analyzed for superelastic properties. The results would be presented at a later point.
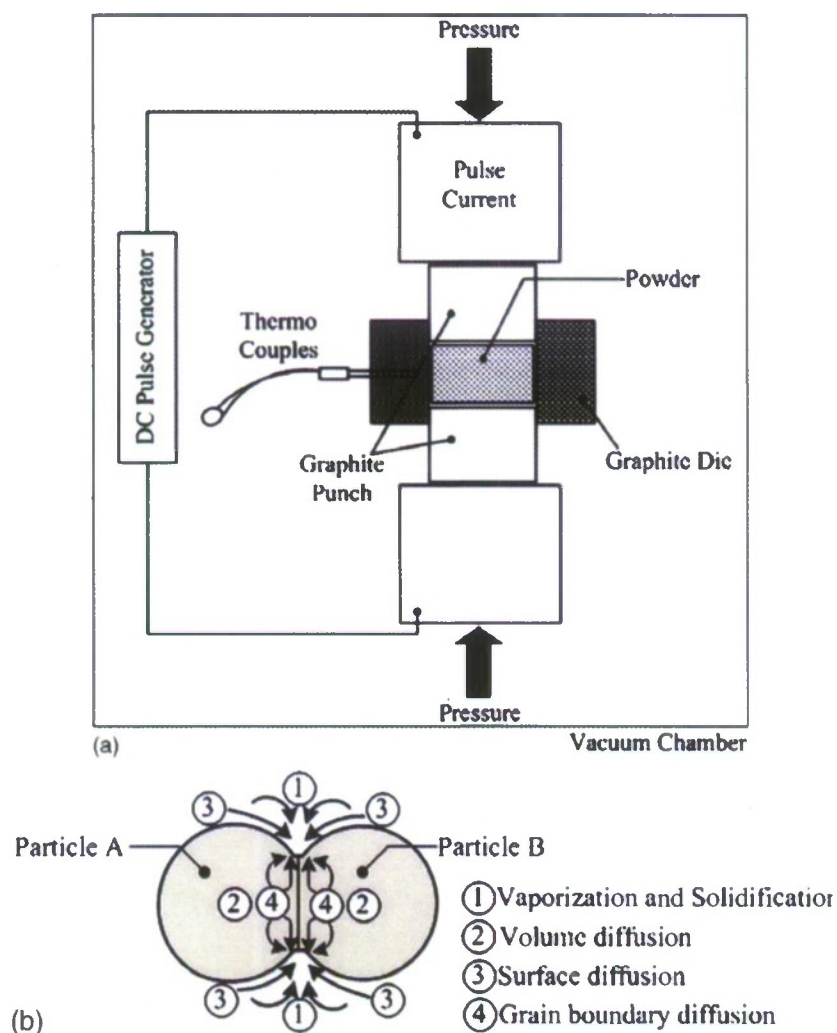

Figure 2.1: Schematic of a) SPS device; and b) SPS process.

Iron metal powders of average particle size of 100 nm were purchased from Argonide Inc. These were processed by Electro-Explosion Wire (EEW) technique. The chemical composition of the iron wire (soft iron) used by Argonide to make the metal powders is: *Mn: 0.78-0.82 %, Cr: <0.1 %, Ni: 0.08-0.098 %, Si: 0.66-0.82 %, Cu: 0.081-0.082 %, V: <0.05 %, Mo: <0.01 %, W: <0.1 % and Carbon* whose content was not determined.

Due to the very small particle size (100 nm), these iron powders are very reactive and special care was taken while handling them. They were stored in vacuum sealed glass vials in a dormant state mixed with hexane. The required weight fractions of iron powder and TiNi powder were taken in a glass vial and acetylene solution was added to it. The glass vial was then put in a Thinky® Mixer for 10 minutes to obtain a homogeneous mixture of powders on evaporation of acetylene.

The presence of acetylene not only aided the mixing process but also prevented the iron powder from getting oxidized. The homogeneous mixture was then placed in the mould and sintering operation was conducted at the set temperature, heating rate and pressure. After sintering, each sample was aged at 320°C for 30 min. This aging condition was chosen based on our previous results documented in Zhao et al 2005.

Table 2.1: Summary of SPS processed TiNi-Fe composites including 100% TiNi specimen

	Sample ID SPS conditions, Composition	Density measured (g/cc)	Theoretical density (g/cc)	Porosity (%)
Nano-sized TiNi powder	600°C x 5 min x 50 MPa, 100K/min pure 51at%TiNi (100 nm) sample	4.16	6.40	35
	800°C x 5 min x 50 MPa, 100K/min pure 51at%TiNi (100 nm) sample	4.90	6.40	23.4
	850°C x 5 min x 50 MPa, 100K/min pure 51at%TiNi (100 nm) sample	5.55	6.40	13.3
	900°C x 5 min x 50 MPa, 100K/min pure 51at%TiNi (100 nm) sample	6.27	6.40	2.0
Micro-sized TiNi powder	600°C x 5 min x 50 MPa, 100K/min, 51at%TiNi (212 μm)+33.33%wt Fe (100 nm)	6.66	6.88	3.2
	700°C x 5 min x 50 MPa,100K/min, 51at%TiNi (212 μm)+33.33%wt Fe (100 nm)	6.65	6.88	3.2
	800°C x 5 min x 50 MPa,100K/min 51at%TiNi (212 μm)+33.33%wt Fe (100 nm)	6.65	6.88	3.2
	700°C x 5 min x 50MPa, 100K/min 51at%TiNi (212 μm)+33.33%wt Fe (74 μm)	6.56	6.88	4.6
	900°C x 5 min x 50 MPa, 100K/min pure 51at%TiNi (212 μm) sample	6.26	6.40	2.1

The results of the SPS processing of TiNi-Fe composites are summarized in Table 2.1. It was not possible to obtain dense samples exhibiting superelasticity using Nano-sized TiNi and Fe powders. The SPS processing pure TiNi samples using the Nano-sized TiNi powders under 900°C, 50 MPa, resulted in high density TiNi specimen with its porosity reduced to 2%. However, Differential Scanning Calorimeter (Perkin Elmer DSC-6) data of this TiNi specimen did not exhibit any shape memory properties. In fact, XRD results of this TiNi specimen showed $TiNi_3$ peaks which persisted after solution quenching, see Fig.2.2 (Allafi 2003). These poor data of TiNi-Fe composite using Nano-sized TiNi powders led us to switch to larger Micro-sized TiNi powers and Nano-sized Fe powders.
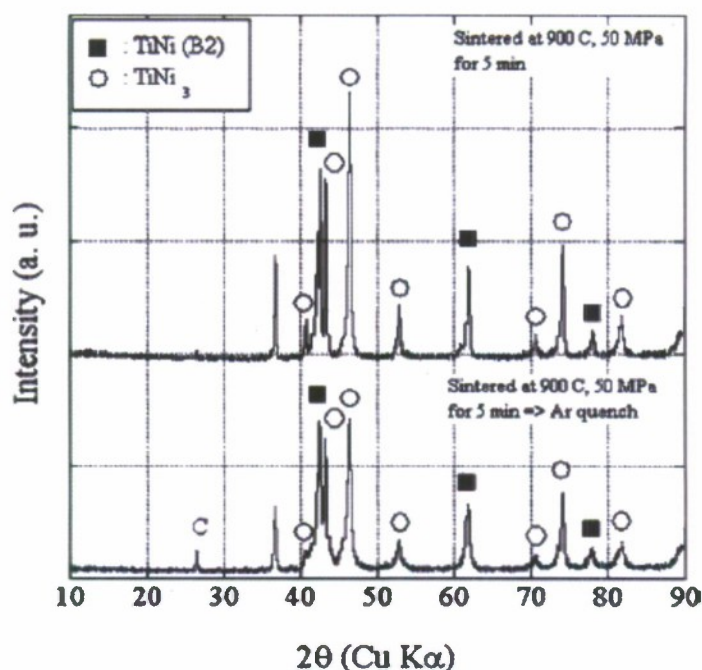
Figure 2.2. XRD data of 900°C x 5 min x 50 MPa, 100K/min pure 51at%TiNi (100 nm) sample.

The results of SPS processed composites using this combination has been shown in the lower half of Table 2.1 where relative densities of 97% and higher were obtained at reasonably low sintering temperatures of around 700°C. The iron particles fill in the gaps between TiNi powders and form the matrix phase of the composite after the sintering operation is completed. The microstructures of these sintered samples (700°C SPS) are characterized using scanning electron microscopy (SEM, T330A Hitachi). Figure 2.3 show SEM images of a finely polished specimen after sintering. Structural compositions of the samples are characterized using X-ray diffraction (XRD). The density is measured using a technique based on Archimedes principle.

Determination of the transformation temperatures was the next step in the material characterization process. This was conducted by DSC tests with a heating/cooling rate of 10°C. DSC experiments of the dense SPS sintered specimen of 30%wt TiNi (212μm diameter) + 70%wt Fe (100nm) processed at 700°C, 5 min sintering time, and 50 MPa pressure revealed the transformation temperatures as A_f (Austenite finish) = 40°C, A_s (Austenite start) = 28°C, M_f (Martensite finish) = 15°C, and M_s (Martensite start) = 30°C. These TiNi-Fe composite specimens were then cut into cylinders of 5 mm diameter using Electrical Discharge Machining (EDM). The specimens were then tested using Instron Model 8562 compression testing equipment. Figure 2.4(b) depicts a typical stress-strain response of TiNi-Fe composite tested at 41°C (which is slightly higher than A_f = 40°C) exhibiting a superelastic loop.
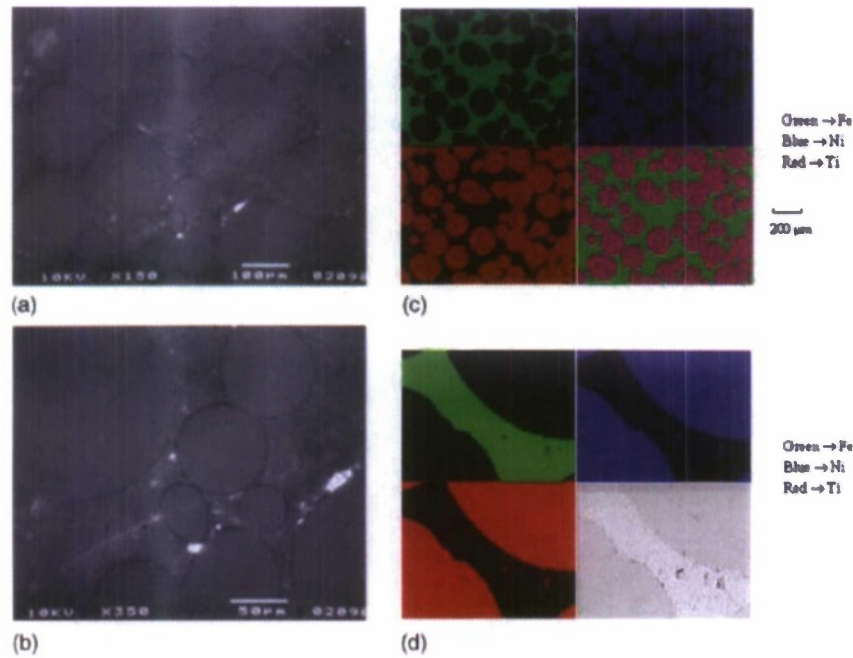
Figure 2.3: (a) and (b) SEM images of 33.33%wtFe (100 nm) + 66.67%wt 51at%TiNi (212 μm) composite; (e) and (d) Composition Maps of the same specimen.
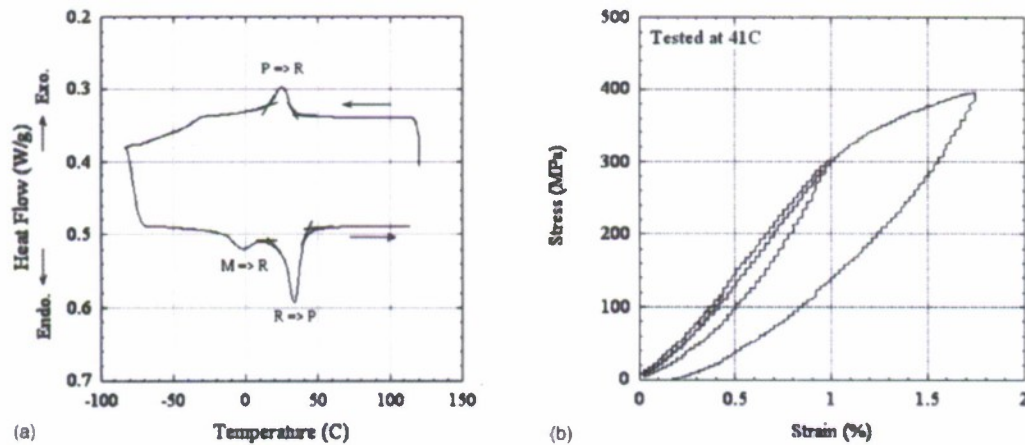
Figure 2.4. TiNi 30 wt % Fe composite specimen with SPS 700°C, 5 min, 50 MPa pressure, then aged at 320°C for 1h experimental results. (a) DSC data yielding A_f=40°C, A_s=28°C, M_s=30°C and M_f=15°C; (b) compression stress-strain curve of this composite specimen at 41°C (=Af), exhibiting to some extent superelastic loop.

2.3. Theoretical Model

2.3.1. Composite Magnetic Permeability

In this section, Eshelby's equivalent inclusion method (Eshelby 1957) in conjunction with Mori-Tanaka's mean-field theory (Mori 1973) has been used to predict the effective magnetic properties (effective magnetic permeability and saturation magnetization) of Fe-TiNi particulate

composite. The first step involved defining a representative volume element of the particulate composite used in this study. To this end, the Fe-phase was chosen as the f-phase or inhomogeniety and the TiNi SMA phase was chosen as the m-phase in the RVE as depicted in Fig.2.5. The implications of such a definition will be discussed at a later point. Thus, the properties of the Fe-phase are represented by subscript 'f' in the evolution of the Eshelby's model while the properties of SMA are denoted by the subscript 'm' as depicted in Fig.2.5. In the absence of inhomogeneties, the matrix SMA phase has the following property

$$B = \mu_m \bullet H_m \tag{2.1}$$

where B is the magnetic flux, H_m is the magnetic field intensity and μ_m is the magnetic permeability of the matrix material respectively. Equation (2.1) is reminiscent of an equivalent stress-strain formulation originally proposed and now widely accepted Eshelby's model. For paramagnetic materials (such as TiNi SMA material), the magnetic susceptibility χ typically lies in the range of $10^{-3} - 10^{-5}$, consequently, the magnetization vector is very weak. Therefore, the magnetic field intensity in the matrix phase takes the following form (Chikazumi 1964):-

$$H_m = H_o + M \Leftrightarrow H_m \approx H_o \tag{2.2}$$

where H_o is the applied magnetic field intensity on the domain under consideration as depicted in Fig.2.5 (a). Essentially, Eq(2) conveys that due to the weak magnetization of paramagnetic materials constituting the particulate phase of the composite domain, the magnetic field intensity of the matrix phase would be equal to the applied magnetic field intensity. Equation (2.2) is valid for most paramagnetic materials such as TiNi for which the magnetization vector $M \approx 0$. Equation (2.1) can thus be written as: -

$$B = \mu_m \cdot H_o \tag{2.3}$$
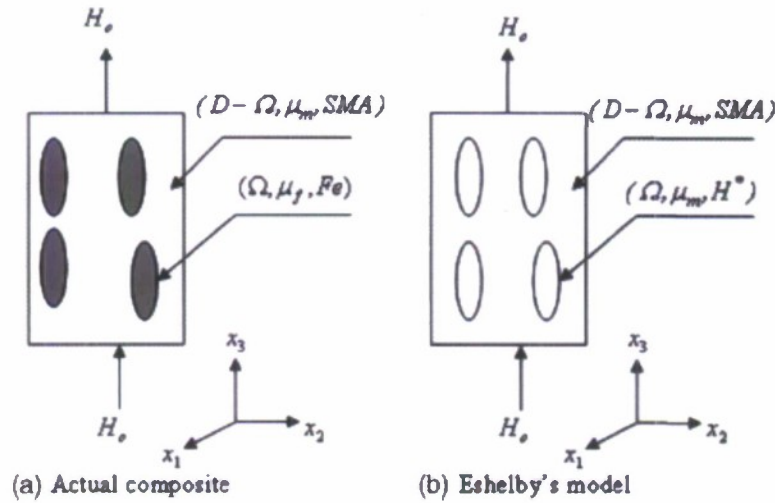
Figure 2.5. Analytical modeling of (a) particulate TiNi-Fe composite where the matrix of shape memory alloys (TiNi SMA) is embedded with ferromagnetic fillers (Fe) is converted to the Eshelby's equivalent inclusion method in (b).

The error associated with neglecting the magnetization for paramagnetic has been found to be of the order of 0.01% which is considered acceptable in the present work (Chikazumi 1964). Upon addition of an inhomogeniety (f-phase), the flux and field vectors are related as follows in Ω (See Fig.2.5):-

$$B + B_d = \mu_f \cdot (H_o + H_d) = \mu_m \cdot (H_o + H_d - H^*) \tag{2.4}$$

8

where B_d and H_d are disturbance flux and field vectors respectively. Physically, H_d represents the demagnetization field characteristic of ferromagnetics. By definition for ferromagnetics,

$$B = \mu_o \cdot (H_o + M - N \cdot M) = \mu_f \cdot (H - N \cdot M) \tag{2.5}$$

where $N \rightarrow$ demagnetization factor, a tensor quantity depending only on the shape of the inhomogeniety, analogous to Eshelby's tensor 'S' of mechanical case. Choosing $H_d = -N \cdot M$ in Equation (2.5) we get,

$$H_d = N \cdot H^* = S^m \cdot H^* \tag{2.6}$$

or,

$$B + B_d = \mu_f \cdot (H_o + S^m \cdot H^*) = \mu_m \cdot (H_o + S^m \cdot H^* - H^*)$$

where '$S^m = N$' has been looked upon as the 'Eshelby tensor' for magnetic case. From Eq(2.6), H^* can be solved. When the volume fraction of ferromagnetic inhomogeneties (f) becomes finite, the interactions between ferromagnetic particles need to be accounted for. This has been accomplished by utilizing Mori-Tanaka's mean-field theory in the present case[1]. $\overline{H}$ has been coined as the average magnetic field and Eq(2.6) is modified as follows taking into account the volume fraction effects:-

$$B + B_d = \mu_f \cdot (H_o + \overline{H} + H_d) = \mu_m \cdot (H_o + \overline{H} + H_d - H^*)$$

$$\text{or, } B_d = \mu_m \cdot (\overline{H} + H_d - H^*) \tag{2.7}$$

Since the volume integration of H_d must vanish over the entire domain, we get,

$$\overline{H} = -f(H_d - H^*) \tag{2.8}$$

Substituting in (2.7) and simplifying gives us,

$$H^* = \left[(\mu_f - \mu_m) \cdot \left\{ (1-f)S^m + fI \right\} + \mu_m \right]^{-1} \cdot (\mu_m - \mu_f) \cdot H_o \tag{2.9}$$

The corresponding concentration factor tensor A can be evaluated as^{Error! Reference source not found.} :-

$$H_f = H_o + \overline{H} + H_d = H_o + H_d(1-f) + fH^* = H_o + \left\{ (1-f)S^m + fI \right\} \cdot H^*$$

$$\text{or, } H_f = A \cdot H_o \tag{2.11}$$

$$\text{with } A = \left[I + \left\{ (1-f)S^m + fI \right\} \cdot \left[(\mu_f - \mu_m) \cdot \left\{ \begin{array}{c} (1-f)S^m + \\ fI \end{array} \right\} + \mu_m \right]^{-1} \cdot (\mu_m - \mu_f) \right]$$

$$\therefore \mu_c = \mu_m + f(\mu_f - \mu_m) \cdot A \tag{2.12}$$

where μ_c represents the effective magnetic permeability of the composite. Therefore, by knowing the properties of the individual constituents of the composite and the geometry of the inclusion, the composite magnetic permeability can be evaluated. The computation of demagnetization factor has been done by many researchers and the values are therefore known (Beleggia 2003, Osborn 1945).

2.3.2. Saturation Magnetization (M_s^c)

The magnetic field intensity in the composite is evaluated as follows[2]:-

$$H_c = (1 - f)\langle H_m \rangle + f\langle H_f \rangle$$

---

[1] Atomic interaction effects have been neglected here.

[2] $\langle \ \rangle$ Denotes volume average over the entire domain.

where $\langle H_m \rangle, \langle H_f \rangle$ are volume averaged quantities. Using the procedure outlined in Electronic Composites book, Taya 2005, the composite magnetic field intensity takes the following form: -

$$H_c = H_o + M_s^c = H_o + fM_s$$

$$\text{or}, M_s^c = fM_s$$

(2.13)

Here, M_s is the saturation magnetization of the ferro-particulate or the f-phase of the composite and M_s^c represents the composite saturation magnetization. Based on this formulation, the magnetization at saturation M_s of TiNi-Fe composites processed at different weight fractions were predicted and compared with the experimental values. The following section outlines the results.

2.4. Results and Conclusions

After characterizing the sintered samples with various volume fractions as shown in Table 2.1, the samples satisfying the key requirements (DSC showing peaks of shape memory properties) were chosen, namely Particulate TiNi/Fe processed by SPS at 700°C in vacuum for 5 minutes and 50MPa with 30, 50 and 70% Fe by weight. The magnetization (**M**) – magnetic field (**H**) curves of the composite specimens were then measured using vibrating specimen magnetometer (VSM) located at Tohoku University in order to compare with the theoretical predictions. The model predictions of saturation magnetization were compared with measured magnetization at saturation resulting in a good match. A comparison of magnetization at saturation (M_s) of TiNi-Fe composites between predictions and experimental data has been summarized in Table 2.2.

Table 2.2. Comparison of predicted magnetization at saturation of TiNi-Fe particulate with measured data.

Weight % of Fe	Volume fraction of Fe[3] (f)	M_s^c (Experimental) (emu/g)	M_s^c (Predicted) (emu/g)
30	0.26133	40	52.266
50	0.4522	93	90.44
70	0.6582	135	131.64
100	1.0	200	200

The results of Table 2.2 have also been plotted in Fig.2.6. Table 2.2 and Fig.2.6 show a good agreement between the experiment and the proposed analytical model despite the fact that at lower weight percents of Fe filler, the predicted M_s^c is slightly overestimated. At lower f, smaller sized Fe particles tend to be distributed along the boundaries of larger sized NiTi particles (Gururaja 2005). At larger f, on the other hand, Fe filler particles become more uniformly distributed to form a continuous matrix, similar to the model configuration, Fig.2.5 (a). Therefore, for lower f, the predicted values of M_s^c deviate slightly from the experimental data while for larger f, we see a very good agreement as evidenced in Table 2.2 and Fig.2.6.

---

[3] $f = \dfrac{1}{1 + \dfrac{1-w}{w} \dfrac{\rho_{Fe}}{\rho_{NiTi}}}$; $\rho_{Fe}, \rho_{NiTi} \rightarrow$ densities of Fe and TiNi (7874 and 6500 g/cc respectively)
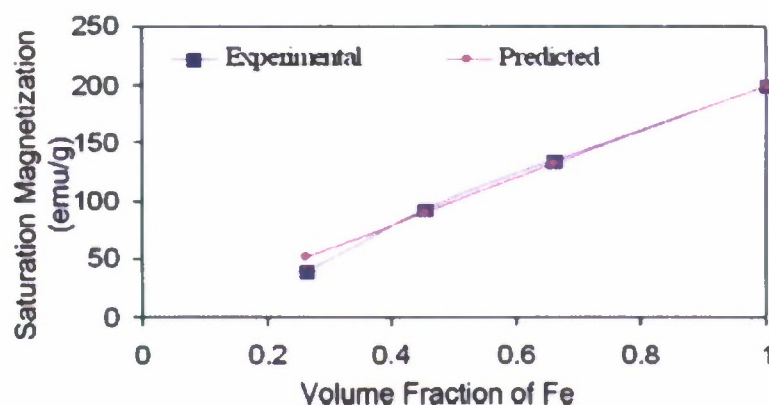
Figure 2.6. Comparison of saturation magnetization (M_s) of TiNi-Fe particulate composites as a function of Fe predicted by the Eshelby's model (shown as filled circular symbols) and experimental data (filled square symbols).

The present model is based on Eshelby's effective medium theory (EMT) with Mori-Tanaka's mean field theory, thus its validity is good for the entire range of filler weight (volume) fraction, $0 \leq f \leq 1$. It should further be pointed out here that the average size of NiTi is 212 μm which is considerably larger than that of the constituent Fe powder of 100 nm size. Compositional maps of the particulate composites indicated that the Fe-phase form the matrix phase of the composite unlike the model presented in Fig.2.5. The implications of this discrepancy needs to be investigated further and shall be looked into in future studies. However, despite this assumption, as mentioned previously, the predictions seem to match with the observed experimental values.

The combination of Micro-sized TiNi powders and Nano-sized Fe powders resulted in the formation of high density specimens which exhibited superior stress-strain characteristics. Nano-sized Fe powders tend to fill in the gaps between Micro-sized TiNi powders much better than Micro-sized Fe powders thereby enhancing the bonding resulting in stronger load transference at TiNi-Fe interfaces. Such an interface behavior facilitates the phase transformation demonstrated by the TiNi phase of the composite. This synergy between the two phases of the composite is expected to benefit actuator designers using this particular material system. Several combinations of the Micro-sized TiNi and Nano-sized Fe were chosen and the respective stress-stain curves for each combination were looked upon. Due to obvious space constraints, not all the stress-strain curves have been included in this paper. Instead one representative stress-strain curve demonstrating the phase transformation phenomenon has been included in the present work. The selection of an optimal volume fraction of TiNi and temperature/pressure/duration of SPS process was found to be very critical in the formation of a sample that would exhibit the SMA properties under compression testing. Consequently, series of experiments were conducted to identify these optimal volume fraction and SPS process conditions using a design of experiments approach and a few optimal conditions have been identified. The microstructure of the composite was also studied using SEM and TEM studies.

An extension of Eshelby's method for the determination of effective magnetic properties of an FSMA system has been proposed in the present paper and the predicted results were compared with experimental results leading to a validation of the proposed model.

Chapter 3.   Modeling of Piezoelectric - Shape Memory Alloy (SMA) Composite as a Fast Responsive Actuator Material

A hybrid composite of a piezoelectric ceramic and shape memory alloy (SMA) is proposed as a new actuator material with fast actuation speed and large strain. Analytical modeling of the composite is constructed based on Eshelby theory where linear piezoelectric constitutive equations and bi-linear super-elastic equations of SMA are used. The predictions of the strain induced by applied stress and electric field are also modeled with two simple designs of piezo-SMA composites, 1-D series and 1-D parallel laminated composites. The predictions based on the proposed model indicate that 1-D parallel laminate provides the highest strain induced under bias stress and applied electric field among other composite geometries examined.

Piezoelectric materials and shape memory alloys (SMAs) are very common materials for actuators and sensors. In the conventional actuator materials, the speed of actuation and sensing is fast, but the order of induced strain is modest while the latter exhibits larger strain, but at much slower speed of actuation. Shape memory alloy (SMA) of super elastic grade has a large strain (up to 5% or so) once it is stressed to the stress level of stress-induced martensite transformation, while piezoelectrics exhibits small-strain (typically less than 1%) with fast actuation speed under applied electric filed. If the above two materials are combined to form a composite, which is termed as piezo-SMA composite, one would expect some unique property to arise. Several researchers Dunn and Taya (1993a; 1993b), Kuo and Huang (1997); Odegard (2004); Qin (2004) predicted that the electromechanical properties of piezoelectric composites consist of piezo matrix and non-piezo filler. The concept of piezo-SMA composite was considered by Jiang and Batra (2002) who formulated the composite model by considering the piezo and SMA phases as filler, which are embedded in isotropic polymer matrix and the Eshelby's method in their analysis. This study, on the other hand, analyzes piezo SMA composite where piezo phase is treated as the matrix and SMA as filler, which can undergo phase-change such as stress-induced martensite transformation as this requires use of Eshelby's method.

In the following, first the Eshelby's method for piezo-SMA composite in general terms will be discussed, then, One-dimensional parallel model will be introduced to examine the piezo-SMA as an actuator.

3.1. Modeling Electromechanical Coupling with Eshelby's Theory

The mechanical and electrical behavior of a piezoelectric material can be modeled by two linearized constitutive equations. These equations contain two mechanical and two electrical variables. The direct effect can be modeled by following matrix equations [IEEE standard on Piezoelectricity, ANSI standard 176-1987]:

$$\sigma_{ij} = C_{ijmn}\varepsilon_{mn} + e_{nij}(-E_n) \tag{3.1}$$

$$D_i = e_{imn}\varepsilon_{mn} - \kappa_{in}(-E_n) \tag{3.2}$$

The constitutive equations for a linear piezoelectric material cab be represented in matrix notation as, see Dunn and Taya (1993a; 1993b), Taya (2005)

$$\Sigma = RZ \tag{3.3}$$

where Σ represent flux tensor of 9x1, the first six column vector components are the stress components, and the last three are electric displacement. Z is the field tensor of 9x1, the first six column vector components are elastic strain, and the last three vector components are electric

field. $\mathbf{R}$ is the electro-elastic property tensor of 9x9. Flux, field and electro-elastic property tensors can be represented as

$$\Sigma = \begin{bmatrix} \sigma_{6x1} \\ \mathbf{D}_{3x1} \end{bmatrix}, \ \mathbf{Z} = \begin{bmatrix} \varepsilon \\ -\mathbf{E} \end{bmatrix}, \ \mathbf{R} = \begin{bmatrix} \mathbf{C} & \mathbf{e}^T \\ \mathbf{e} & -\kappa \end{bmatrix} \tag{3.4}$$

respectively, where σ, $\mathbf{D}$, $\mathbf{C}$, $\mathbf{e}$, κ, ε, and $\mathbf{E}$ denote stress, electric displacement, elastic moduli, piezoelectric constants, dielectric constants, strain, and electric field matrices, respectively. Piezo phase is assumed as a transversely isotropic piezoelectric solid.

Consider an Eshelby model for a piezoelectric material. The composite of interest consists of an infinite piezoelectric matrix ($D - \Omega$) containing a finite volume fraction, f, of spheroidal SMA fillers (Ω), as shown in Fig.3.1(a). The SMA fillers are considered as non-piezoelectric, but exhibit a bi-linear stress-strain curve, that reflects the stress-induced phase transformation. The fillers have electro-elastic modulus $\mathbf{R}_f$ while the matrix has electro-elastic modulus $\mathbf{R}_m$.
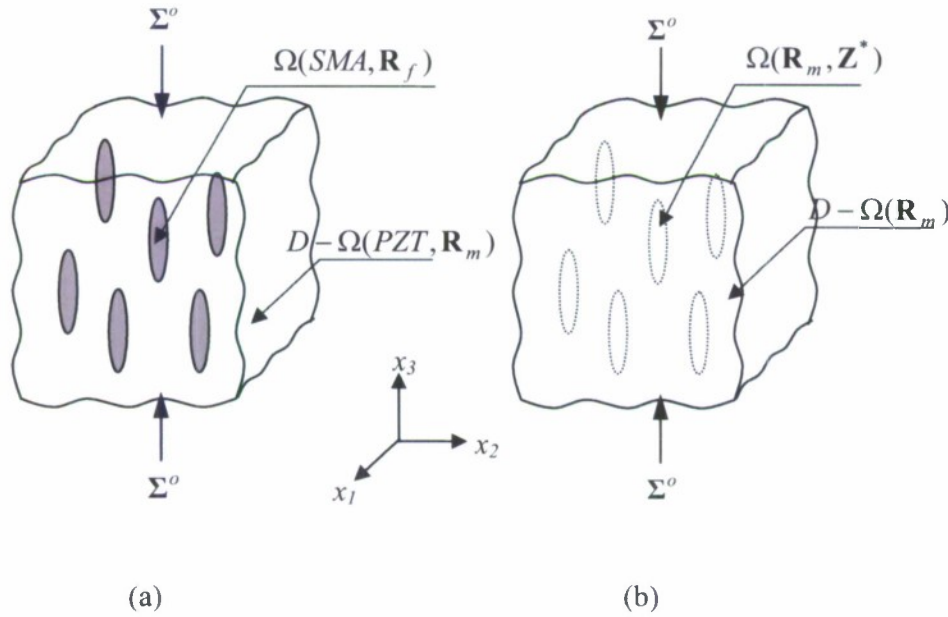

Figure 3.1. Analytical model for piezoelectric composite containing non-piezoelectric SMA fillers, (a) original problem, which is converted to (b) Eshelby's equivalent inclusion problem.

The composite is subjected to the far-field uniform applied stress and electric displacement Σ^o. Fillers in the piezoelectric matrix can be simulated by equivalent inclusions, resulting in Fig.3.1(b) where the electro-elastic stiffness tensor $\mathbf{R}_m$ is homogeneous in the entire domain (D).

When a piezo-SMA composite is subjected to a far-field uniform flux vector (applied stress and electric displacement) Σ^o, the flux vector (stress and electric displacement) in the filler, Σ_f, can be written as

$$\Sigma_f = \mathbf{R}_f\left(\mathbf{Z}^o + \overline{\mathbf{Z}} + \mathbf{Z}\right) = \mathbf{R}_m\left(\mathbf{Z}^o + \overline{\mathbf{Z}} + \mathbf{Z} - \mathbf{Z}^*\right) \tag{3.4}$$

Where, $\mathbf{Z}$ is the disturbance of the uniform field vector due to the presence of the fillers and $\overline{\mathbf{Z}}$ is the average disturbance of the field vector (strain and electric field) in the matrix. $\mathbf{Z}^*$ is the fictitious eigen field vector (eigen strain and eigen electric field) by means of equivalent inclusion method. $\mathbf{Z}^o$ is the uniform field vector (strain and electric field) provided by uniform flux vector, Σ^o that would exist in the absence of the filler and they are related as

$$\Sigma^o = \mathbf{R}_m\mathbf{Z}^o \tag{3.5}$$

The flux vector (stress and electric displacement) in the matrix, Σ_m, can be written as

$$\Sigma_m = \mathbf{R}_m\left(\mathbf{Z}^o + \overline{\mathbf{Z}}\right) \tag{3.6}$$

The disturbed field vector (strain and electric field) in the filler, $\mathbf{Z}$, is related with fictitious eigenfield vector $\mathbf{Z}^*$ through a piezoelectric Eshelby tensor $\mathbf{S}$ as

$$\mathbf{Z} = \mathbf{S}\mathbf{Z}^* \tag{3.7}$$

The flux boundary condition (Σ^o) and the volume integral of the disturbance flux vector (being zero over the entire composite domain) leads to the following relation that relates $\overline{\mathbf{Z}}$ to $\mathbf{Z}$ and $\mathbf{Z}^*$ as

$$\overline{\mathbf{Z}} + f\left(\mathbf{Z} - \mathbf{Z}^*\right) = 0 \tag{3.8}$$

where f denotes the volume fraction of the SMA fillers. $\mathbf{Z}^*$ is computed from Eqs.(3.4,3.5,3.7 and 3.8) as

$$\mathbf{Z}^* = \mathbf{B}\left(\mathbf{R}_m - \mathbf{R}_f\right)\mathbf{Z}^o \tag{3.9}$$

$$\mathbf{B} = \left\{\left(\mathbf{R}_f - \mathbf{R}_m\right)\left[(1 - f)\mathbf{S} + f\,\mathbf{I}\right] + \mathbf{R}_m\right\}^{-1} \tag{3.10}$$

where $\mathbf{I}$ is 9×9 identity matrix and the superscript of "-1" denotes inverse of matrix.

The overall field vector (strain and electric field) of the composite $\mathbf{Z}_c$ is computed by using the weighted volume average (rule of mixture) of that over each phase and given by

$$\mathbf{Z}_c = (1 - f)\mathbf{Z}_m + f\mathbf{Z}_f = \left[\mathbf{I} + f\,\mathbf{B}\left(\mathbf{R}_m - \mathbf{R}_f\right)\right]\mathbf{Z}^o \tag{3.11}$$

where $\mathbf{Z}_m$ and $\mathbf{Z}_f$ represent total field vectors (strain and electric fields) in the matrix and filler, respectively. The total flux vectors (stress and electric displacement) of each component are expressed as

$$\Sigma_f = \left[\mathbf{R}_m - (1-f) \cdot \mathbf{R}_m \cdot (\mathbf{S} - \mathbf{I}) \cdot \mathbf{B} \cdot (\mathbf{R}_f - \mathbf{R}_m) \right] \cdot \mathbf{R}_m^{-1} \cdot \Sigma^o \tag{3.12a}$$

$$\Sigma_m = \left[\mathbf{R}_m + f \cdot \mathbf{R}_m (\mathbf{S} - \mathbf{I}) \cdot \mathbf{B} \cdot (\mathbf{R}_f - \mathbf{R}_m) \right] \cdot \mathbf{R}_m^{-1} \cdot \Sigma^o \tag{3.12b}$$

The overall flux vector (stress and electric displacement) of the composite is then given by

$$\Sigma_c = (1-f)\Sigma_m + f\,\Sigma_f = \Sigma^o \tag{3.13}$$

The effective electro-elastic modulus of the composite $\mathbf{R}_c$ is defined as

$$\Sigma_c = \mathbf{R}_c \mathbf{Z}_c \tag{3.14}$$

From Eqs.(3.5, 3.11, 3.13, and 3.14) the effective electro-elastic modulus of the composite is obtained as

$$\mathbf{R}_c = \mathbf{R}_m \left[\mathbf{I} + f\,\mathbf{B}(\mathbf{R}_m - \mathbf{R}_f) \right]^{-1} \tag{3.15}$$

3.1.1. Mixed Boundary Condition Problem

When a composite is subject to applied stress $\boldsymbol{\sigma}^o$ and an electric field $\mathbf{E}^o$, where $\boldsymbol{\sigma}^o$ is a part of flux vector and $\mathbf{E}^o$ is a part of field vector, see Eqs.(3.1, 3.2), this lead the problem to have a mixed boundary condition. Mixed boundary condition should be converted to the non-mixed boundary condition in order to apply the Eshelby's equivalent inclusion method discussed in the previous section. This can be done by using the effective properties of the composite derived in the previous section, Eq.(3.15).

Equation (3.1) for strain can be rewritten in terms of the composite properties the strain in the composite can be computed as

$$\boldsymbol{\varepsilon}_c = \mathbf{C}_c^{-1}\boldsymbol{\sigma}^o + \mathbf{C}_c^{-1}\mathbf{e}_c^T\mathbf{E}^o \tag{3.16}$$

where the subscript "c" denotes the composite material properties.

The electric displacement generated in the composite by applied mixed boundary condition ($\boldsymbol{\sigma}^o$ and $\mathbf{E}^o$) can be obtained by substituting Eq.(3.16) in to Eq.(3.2)

$$\mathbf{D}_c = \mathbf{e}_c\mathbf{C}_c^{-1}\boldsymbol{\sigma}^o + \mathbf{e}_c\mathbf{C}_c^{-1}\mathbf{e}_c^T\mathbf{E}^o + \boldsymbol{\kappa}_c\mathbf{E}^o \tag{3.17}$$

By using the applied stress ($\boldsymbol{\sigma}^o$) and Eq.(3.17), the mixed boundary condition can be converted to the non-mixed boundary condition represented as

$$\Sigma^o = \begin{bmatrix} \boldsymbol{\sigma}_c \\ \mathbf{D}_c \end{bmatrix} = \begin{bmatrix} \boldsymbol{\sigma}^o \\ \mathbf{e}_c\mathbf{C}_c^{-1}\boldsymbol{\sigma}^o + \mathbf{e}_c\mathbf{C}_c^{-1}\mathbf{e}_c^T\mathbf{E}^o + \boldsymbol{\kappa}_c\mathbf{E}^o \end{bmatrix} \tag{3.18}$$

3.1.2. Stress only Boundary Condition

We shall consider the composite subjected to the applied stress in absence of electric field, $\boldsymbol{\sigma}^o = \mathbf{U} \cdot \sigma^o$, where $\mathbf{U}$ is defined by

$$\mathbf{U} = \begin{bmatrix} 0 & 0 & 1 & 0 & 0 & 0 \end{bmatrix}^T \tag{3.19}$$

The magnitude of the initial stress applied to the composite is just to initiate stress-induced martensite transformation of the SMA fillers σ_{ms} (see Fig.3.2). The boundary condition for this case is obtained from Eq.(3.18) can be written in terms of stress magnitude σ^o as;

$$\Sigma^o = \mathbf{U}_{\Sigma^o}\sigma^o \tag{3.20}$$

where $\mathbf{U}_{\Sigma^o}$ is 9 x 1 column vector and given by

$$\mathbf{U}_{\Sigma^o} = \begin{bmatrix} \mathbf{U} \\ \mathbf{e}_c \mathbf{C}_c^{-1} \mathbf{U} \end{bmatrix} \tag{3.21}$$

When the composite is subjected to a far-field uniform flux vector (stress and electric displacement), Σ^o, field vector (the stress and electric displacement) in the filler, Σ_f, can be computed by Eq.(3.12a). It is simply rewritten as

$$\Sigma_f = \mathbf{U}_{\Sigma f}\sigma^o \tag{3.22}$$

where

$$\mathbf{U}_{\Sigma f} = \left[\mathbf{R}_m - (1-f)\cdot\mathbf{R}_m(\mathbf{S}-\mathbf{I})\cdot\mathbf{B}\cdot\left(\mathbf{R}_f - \mathbf{R}_m\right)\right]\cdot\mathbf{R}_m^{-1}\cdot\mathbf{U}_{\Sigma^o} \tag{3.23}$$

The magnitude of initially applied stress that initiates austenite to martensite transformation of the fibers is called bias stress and denoted as σ_{ms}^o. The bias stress can be determined by using Von-Mises effective stress, σ_{eff}, defined in the SMA filler domain which is equal to the martensite start stress, σ_{ms} [Taya and Arsenault, 1989]

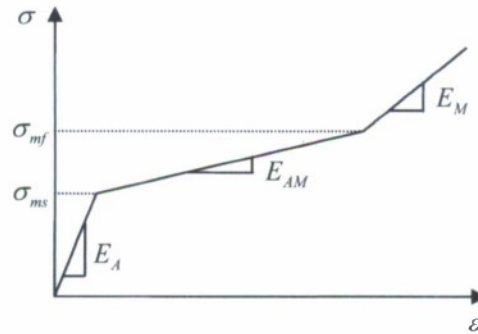$$\sigma_{eff} = \sigma_{ms} = \Sigma_{f,33} - \Sigma_{f,11} \tag{3.24}$$

Figure 3.2 Bi-linear stress-strain curve of SMA.

where subscripts "33" and "11" represent the components of the vector Σ_f, along the SMA fiber axis $(x_3-$ axis) and its transverse direction, respectively.

From Eq.(3.22) and (3.24), the bias stress can be obtained as

$$\sigma^o_{ms} = \frac{\sigma_{ms}}{\mathbf{U}_{\Sigma f,33} - \mathbf{U}_{\Sigma f,11}} \tag{3.25}$$

where σ_{ms} represents the martensite start stress of the SMA filler, see Fig.3.2.

Under this boundary condition, the bias strain in the composite after applying the bias stress can be computed by Eq. (3.14).

3.1.3. E-Field Boundary Condition

During the transformation of SMA fiber, from austenite to martensite, the relation between stress and strain of the SMA filler is assumed to be linear between σ_{ms} and σ_{mf} (see Fig.3.2). The applied stress is kept to be constant and its magnitude is computed from Eq.(3.25), while electric field $\mathbf{E}$ is varied. The electric field is then increased such that SMA fillers start to transform from austenite to martensite. When both the stress and electric field are imposed on the composite, the problem can be divided into two sub problems. The first stage is the composite subjected to the applied stress described in the previous section (stress only boundary condition). The second stage is the composite subjected to the applied electric field which can be superimposed on the results of the first solution. The analyze of the second stage will be discussed in this section with an arbitrary electric field, $\mathbf{E} = \mathbf{Y} \cdot E^o$, where $\mathbf{Y}$ is defined by

$$\mathbf{Y} = \begin{bmatrix} 0 & 0 & 1 \end{bmatrix} \tag{3.26}$$

The mixed boundary condition is converted into non-mixed boundary condition by Eq.(3.18)

$$\Sigma^o = \begin{bmatrix} \mathbf{0} \\ \mathbf{e}_c \mathbf{C}_c^{-1} \mathbf{e}_c^\mathsf{T} \mathbf{Y} + \mathbf{\kappa}_c \mathbf{Y} \end{bmatrix} E^o = \mathbf{Y}_{E^o} E^o \tag{3.27}$$

The flux vector (stress and electric displacement) in the filler domain is computed by Eq.(3.12a), which is rewritten as

$$\Sigma_f = \mathbf{Y}_{\Sigma f, E^o} E^o \tag{3.28}$$

where

$$\mathbf{Y}_{\Sigma f, E^o} = \left[\mathbf{R}_m - (1-f) \cdot \mathbf{R}_m \cdot (\mathbf{S} - \mathbf{I}) \cdot \mathbf{B} \cdot \left(\mathbf{R}_f - \mathbf{R}_m \right) \right] \cdot \mathbf{R}_m^{-1} \cdot \mathbf{Y}_{E^o} \tag{3.29}$$

By using the definition of effective stress and Eq.(3.28), the magnitude of applied electric field (E^o_{mf}) for the fillers to reach the martensite finish (σ_{mf}), is determined as

$$E^o_{mf} = \frac{\sigma_{mf}}{\mathbf{Y}_{\Sigma f, E^o, 33} - \mathbf{Y}_{\Sigma f, E^o, 11}} \tag{3.30}$$

After substituting computed E^o_{mf} into Eq.(3.27) the total strain of the composite with SMA fillers fully transformed to martensite is computed under, applied electric field, $\mathbf{E}$ only by using Eq.(3.14). Finally, the total strain induced in the composite by both bias stress and electric field is the sum of the strains induced by the results obtained in stress only boundary condition and Electric field only boundary condition.

3.2. One-dimensional model based on parallel connection (1-D parallel model)

Next, we shall discuss one-dimensional model, i.e. 1-D parallel model as shown in Fig.3.3 where the composite is subjected to applied stress σ^o. The free body diagram of the composite is shown in Fig.3.4, where each layer is subjected to internal force.
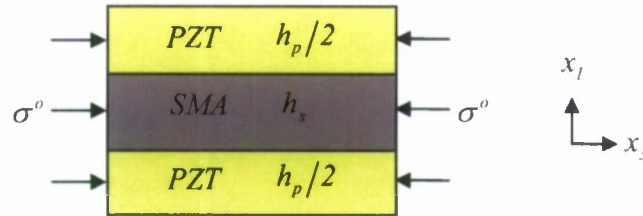

Figure 3.3. Composite with 1-D parallel connection is subjected to applied stress, where h_s and h_p represent the thicknesses of SMA-phase and piezo-phase, respectively.
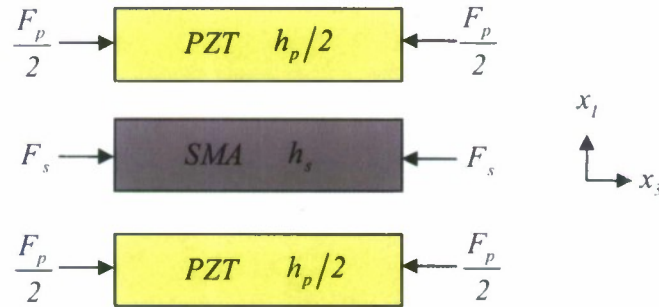

Figure 3.4. Free-body diagram showing forces acting on piezo- and SMA layers of 1-D parallel model.

3.2.1. Analysis of a composite under applied stress σ^o only

The total force acting on the composite is the sum of forces acting on each phase, from which the applied stress σ^o can be expressed as

$$\sigma^o = \frac{F_s + F_p}{h_s + h_p} \tag{3.31}$$

The strains in each phase are obtained from force, Young's modulus, and thickness, which are given by

$$\varepsilon_s = \frac{\sigma_s}{E_s} = \frac{F_s}{E_s h_s} \tag{3.32a}$$

$$\varepsilon_p = \frac{\sigma_p}{E_p} = \frac{F_p}{E_p h_p} \tag{3.32b}$$

Iso-strain condition of this 1-D parallel model ($\varepsilon_s = \varepsilon_p$) gives the relationship between stresses in SMA and PZT phases:

$$\sigma_p = \frac{E_p}{E_s} \sigma_s \tag{3.33}$$

From Eqs.(3.31 and 3.33), the applied stress σ^o can be simply related with the effective stress of SMA filler σ_s as

$$\sigma^o = \sigma_s \frac{fE_s + (1-f)E_p}{E_s} \tag{3.34}$$

The applied stress (σ_{bias}) to start martensite transformation of SMA fibers is obtained from Eq.(3.34) as

$$\sigma_{bias} = \sigma_{ms} \frac{fE_s + (1-f)E_p}{E_s} \tag{3.35}$$

where σ_{ms} is the martensite start stress of SMA. The strain induced in the composite is called bias strain ε_{bias} and is given by

$$\varepsilon_{bias} = \frac{\sigma_{ms}}{E_s} \tag{3.36}$$

where ε_{bias} is the strain corresponding to the applied stress that makes the SMA phase reaching σ_{ms}, see Fig.3.2.

3.2.2. Analysis of a composite under both applied stress σ^o and electric field $\mathbf{E}^o$

Next, let's consider the composite additionally subjected to electric field $\mathbf{E}^o$ based on Fig.3.3. With an addition of electric field $\mathbf{E}^o$ so as to induce the compressive strain in the piezo layer, the stress field in the composite is changed as shown in Fig.3.5. The piezo-phase and SMA are in tension and compression, respectively.
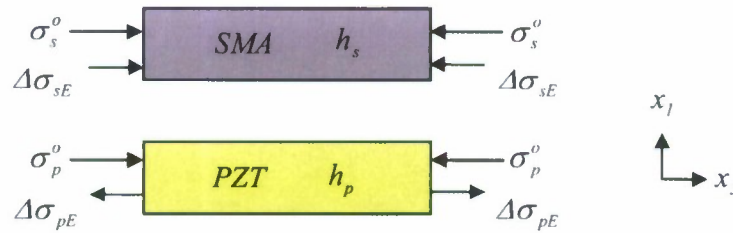

Figure 3.5. Free-body diagram of the composite with applied stress and electric field.

The stress increments in both phases are computed from force equilibrium along the x_3–axis over the entire composite satisfy

$$h_p \Delta\sigma_{pE} = h_s \Delta\sigma_{sE} \tag{3.37}$$

The total strains in both phases are generated by the applied stress and electric field and are the same:

$$\varepsilon_{bias} + \Delta\varepsilon_{sE} = \varepsilon_{bias} + \Delta\varepsilon_{pE} \tag{3.38}$$

The strains in the SMA and PZT due to the applied electric field are expressed as

$$\Delta\varepsilon_{sE} = \frac{\Delta\sigma_{sE}}{E_{AM}}, \qquad \Delta\varepsilon_{pE} = -\frac{\Delta\sigma_{pE}}{E_p} + d_{33}E_3, \tag{3.39}$$

where E_{AM} is Young's modulus of SMA during stress-induced phase transformation, see Fig.3.2. Since the bias strains in both phases are the same, the rearrangement of Eq.(3.38) and Eq.(3.39) results in

$$\frac{\Delta\sigma_{sE}}{E_{AM}} = -\frac{\Delta\sigma_{pE}}{E_p} + d_{33}E_3 \tag{3.40}$$

Since the internal stresses in both phases are balanced out, the changes of the stresses in the phases are related with

$$\Delta\sigma_{sE} = \frac{1-f}{f}\Delta\sigma_{pE} \tag{3.41}$$

By inserting Eq.(3.41) into Eq.(3.40), the stress change in the PZT is obtained as

$$\Delta\sigma_{pE} = \frac{fE_{AM}E_p d_{33}E_3}{fE_{AM} + (1-f)E_p} \tag{3.42}$$

The strain induced in the composite by both bias stress and electric field is obtained as

$$\varepsilon_c = \varepsilon_{bias} + \frac{(1-f)E_p d_{33}E_3}{fE_{AM} + (1-f)E_p} \tag{3.43}$$

3.3. Experimental Study: SPS Process to form Piezo-SMA Composite Material

Once the modeling is complete for the experimental study, Spark Plasma Sintering (SPS) process is used in order to form mechanical bonding between piezo and SMA which will form laminated composite material discussed in modeling part for the actuator.

We attempted to tailor piezo-SMA laminated composite first using powders of piezo and SMA (NiTi), Fig.3.7(a). However, piezo powders (PMN) were oxidized during high temperature SPS process, losing piezo properties. In order to recover the piezo properties, we had to apply reduction process, i.e. heat treatment in a reducing environment to recover the piezoelectric properties which had been destroyed upon heating over the Curie temperature. This post heat treatment in reducing environment resulted in the composite with poor piezo properties. Therefore we tried next by using piezo-plate and NiTi plates stacked together, then subjecting the laminate to SPS process, Fig.3.7(b). The advantage of this method is to keep the original properties of both piezo (PZT) and NiTi plates, while the disadvantage is difficulty of making a stronger bonding between piezo plate and NiTi plate. This method resulted in often in cracking of PZT plate presumably was caused during pressurizing of SPS process, and brittle nature of PZT plate. Therefore, we switched to third method, Fig.3.7(c) where two SMA rings are introduced in the middle layer that constraint PZT piezo disc. In addition, we inserted NiTi powders at the

interface between NiTi plates and Piezo disc. Upon SPS process, the piezo-SMA laminate composite, Fig.3.7(c) appears to be good in shape, no blackening, and no cracking.
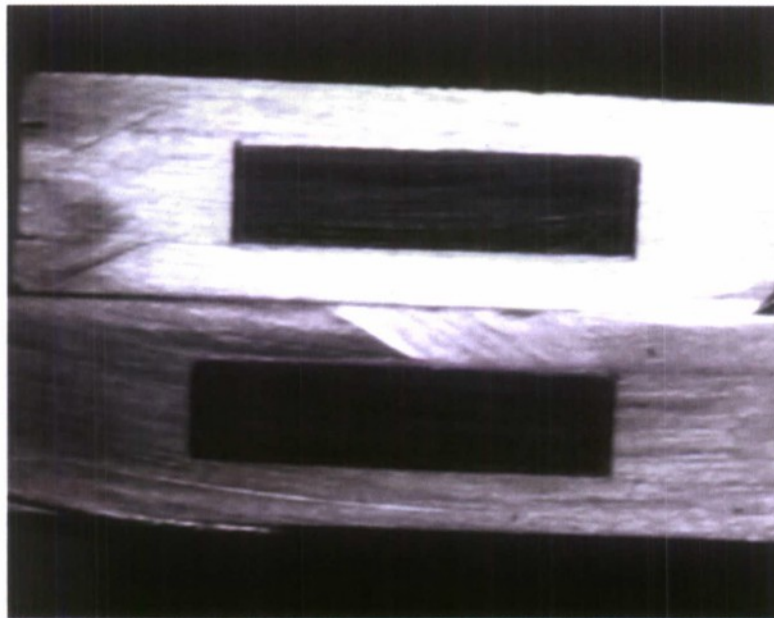

Figure 3.6. Cross section if PZT-NiTi laminated composite processed in case 8 of Table 3.1.

All cases of methods, (a), (b) and (c) in processing of piezo-SMA laminates, are summarized in Table 3.1, where the best piezo-SMA composite is named as case 8. The cross section of case 8 is shown in Fig.3.6.
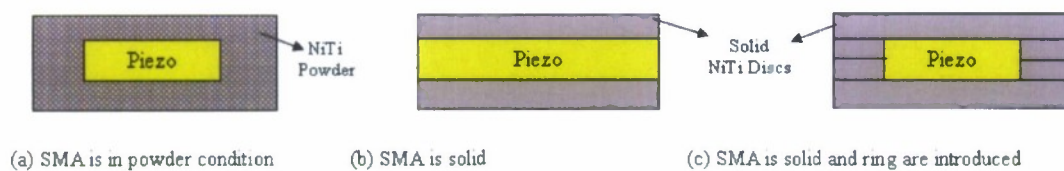

(a) SMA is in powder condition   (b) SMA is solid   (c) SMA is solid and ring are introduced

Figure 3.7. Schematic view for preparing the specimen for SPS process

Table 3.1. Summary of SPS processing on piezo-SMA laminates.

Case	Pressure (MPa)	Heating rate (°C/min), Peak Temp (°C)	Time (min)	Piezo (dia, thickness) mm	NiTi disc, (dia, thick) mm	NiTi ring, thick. mm	Setup (Fig.3.7)	Results
1	1.60	100, 800	5	PMN (20, 1.05)	Powder	N/A	a	PMN color is OK. Several axial cracks. Low porosity, due to fine powder.
2	12	100, 800	5	PZT (10, 2.05)	(10, 1)	N/A	b	PZT is broken. Pressure is high.
3	3.6	100, 800	5	PMN (20, 1.05)	(20,1)	N/A	b	PMN is broken; one surface is bounded well, while the other is not. PMN get black in color.
4	7.96	100, 800	5	PZT (10, 2.05)	(30, 1)	2x1	c	PZT is broken. Rings are not bounded; also PZT is not bounded to NiTi. Surface polishing should be better.
5	4.6	100, 800	5	PZT (10, 2.05)	(30, 1)	2x1	c	Total thickness of the rings is equal to the PZT thickness. PZT is broken. Bounding is OK, between PZT and NiTi.
6	0.80	100, 800	5	PMN (20, 1.05)	Powder	N/A	a	Low range pressure is used for the first time. Only one crack observed in the axial direction. High porosity due to thick powder.
7	1.11	100, 700	5	PMN (20, 1.05)	(20,1)	N/A	b	PMN is broken on purpose before SPS in order to figure out difference in color trough the cracks. After the experiment, it is observed that, some axial and radial cracks; color is black so the difference can not be observed. One side is bounded well while the other is not.
8	1.11	100, 700	5	PZT (10, 2.05)	(30, 1)	2x1	c	Low range loading, PZT with 2.05 mm thickness is used. Fine powder is applied in the gaps between the PZT and Discs due to the thickness difference in PZT and Rings. Also fine powder is applied between NiTi contact layers. Color is OK. No cracks. Bounding seems OK, but should be examined by removing the solid NiTi parts.

3.4. Results and Discussion

In this section of the study, the modeled composites are assumed to be composed of SMA (CuMnAl) fillers and piezo (PZT) matrix, whose properties are given in Table 3.2 [Takagi et al, 2002]. The data marked by * are not available from the literature and assumed with comparing the materials listed in other literature mentioning the same materials. One-dimensional parallel and three dimensional with Eshelby theory are employed with the material properties given. The fillers for Eshelby model are assumed to be continuous SMA fiber where the aspect ratio of prolate ellipsoidal inclusion is set to infinity. Mixed boundary condition is converted into non-mixed boundary condition by using electromechanical coupling behavior of piezoelectric material. Strain in the composite with respect to applied electric field is predicted with two models.

Table 3.2. Property data of piezo and SMA phases.

	C [GPa]					e [C/m^2]			κ	
	C_{11}	C_{12}	C_{13}	C_{33}	C_{44}	e_{31}	e_{33}	e_{15}	κ_{11}/κ_0**	κ_{33}/κ_0
PZT	146	95.4	94.3	128	25.3	-3.94	17.5	12.3*	916*	1654
SMA	$E_A = 29.5$, $E_{AM} = 1.78$, $E_M = 5.75$, $v = 0.3$ $\sigma_{ms} = 117\,MPa$, $\sigma_{mf} = 217\,MPa$						-			

*: not available

** $\kappa_0 = 8.85 \times 10^{-12} [C^2/Nm^2] =$ permittivity of free space

Total strain in the composite with respect to applied electric field is predicted with using 1D parallel model and 3D model with Eshelby theory. Figure 3.8 shows the predicted results for the total strain. The result of 1-D parallel model is close to those of the Eshelby's model with infinite aspect ratio of SMA fibers, which shows a linear relationship between Strain and Electric-Field. Parallel model predicts 10% larger strain then the 3D model which is due to neglecting Poisson's effect associated with the materials. Both strain response starts with a bias strain due to applied bias stress which was defined as; the stress to be applied to the composite in order to have SMA to reach martensite starting condition. This stress value is defined as σ_{mf} in bilinear stress strain curve of SMA.
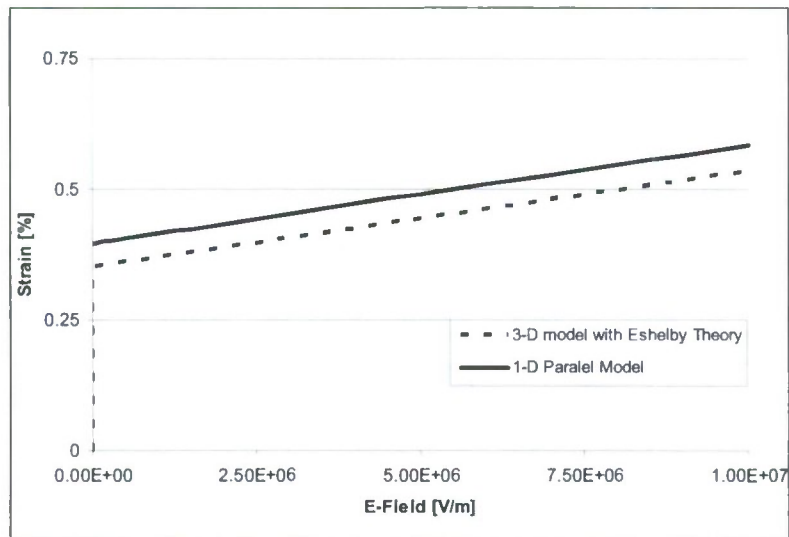
Figure 3.8. Total strain of the piezo-SMA composite with applied electric field

The strain response with different volume fractions of SMA phase is also examined by using 3D model with Eshelby Theory. Figure 3.9 shows the volume fraction of three values; 0.1, 0.2 and 0.3 respectively. As the volume fraction of SMA phase increases the electric field needed to reach same amount of strain is also increasing. This can be interpreted in two ways; one can tell that since the volume fraction of piezo phase is decreasing the stress generated by piezoelectric material is also decreasing with the same amount of electric field applied. On the other hand, since SMA volume fraction is increasing there is more need of stress to trigger stress induced martensitic transformation.
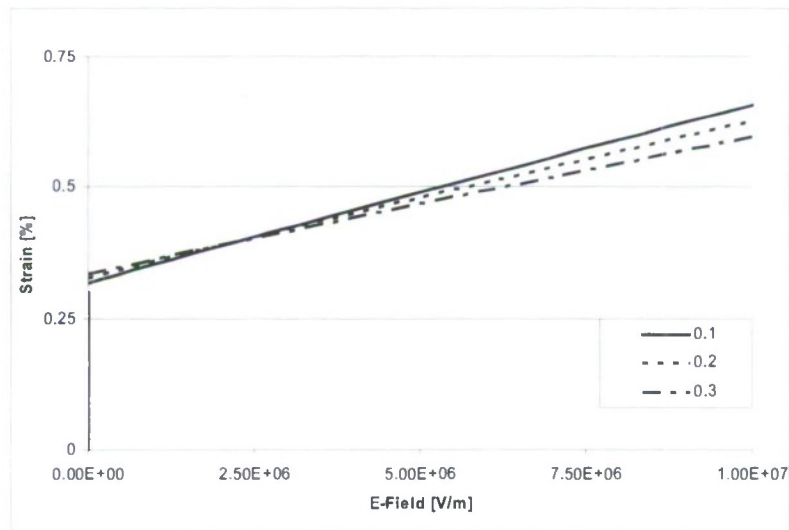

Figure 3.9. Total strain of the piezo-SMA composite with applied electric field for different volume fractions of SMA phase, by using 3D model with Eshelby's theory

A new concept of piezo-SMA composite is proposed as a high performance actuator material under bias stress and applied electric field. The best piezo-SMA composite design for achieving highest strain is use of 1-D parallel composite design of Fig.3.3. To this end, a new analytical model based on Eshelby theory is developed, which can account for anisotropic matrix and linear SMA superelastic behavior. The experimental study is also performed in order to manufacture such a composite where the bonding is required between two phases; piezoelectric material and Shape memory alloy. Spark Plasma Sintering (SPS) machine is used to create such a banding between two materials. In SPS process the pressure and temperature is controlled to achieve the best sintering condition. In addition to several SPS condition, three different design conditions is also tried out as discussed in Experiments section, Fig.3.7. The overall results for SPS are tabulated. In all cases the bonding is examined by nondestructive tests.

Chapter 4.   Piezo-SMA Composite for Thermal Energy Harvesting

Piezoelectric materials and shape memory alloys (SMAs) are very common materials for actuators and sensors; however their composites as electrical generators is least explored, although use of piezoelectric as the mechanical energy harvester is increasingly popular.

Thermal energy harvester using piezo-SMA composite has been designed, where the composite is subjected to fluctuating temperature. The main mechanism of such a piezo-SMA composite is synergistic effect of piezoelectrics and SMA which are connected in series, subjected to fluctuating temperature which induces large straining first in the SMA phase then immediately stressing to the piezoelectric phase, thus, inducing charge by direct piezoelectric effect. In order to make this problem more analytically tractable, we are developing two models, simple laminated model and 3D Eshelby model.

The piezo-SMA composite is made of two plates of piezoelectric ceramic and SMA, which are connected and compressed by the compression spring. The Composite is modeled to have fix displacement boundary condition to ensure the piezoelectric material is in compression throughout the usage. Temperature fluctuation between martensite finish temperature (M_f) and austenite finish temperature (A_f) induces phase transformation in the SMA. Compressive stress is induced during Austenitic transformation; due to heating in SMA phase and fixed displacement boundary condition and compressive stress reduces while SMA transforms to martensitic phase during cooling. The change in the compressive stress is converted in to electrical energy by inverse piezoelectricity. The model predicts the available power according to material properties and thermal fluctuation. The impedance of the system is examined with different thermal fluctuating frequencies. Higher frequencies which result in lower impedance give higher available power to electrical loading. The experimental and predicted results are in agreement for higher frequencies, while for lower frequencies of thermal fluctuation the prediction is not accurate due to internal loss.

4.1. Analytical Model of the Piezo-SMA Energy harvester

Analytical modeling consists of two sections; in the first step stress generated in the composite will be determined with two analytical models; one-dimensional serial composite model, and three-dimensional Eshelby's method; for the second step the corresponding electric field generated by direct piezoelectricity will be calculated. It is convenient to develop analytical

models that can predict the response of composite material made of piezoclectric material and SMA under different input conditions and for known material properties. In this section of the study, for hybrid composite, the analytical modeling is discussed. Stress generated during the thermal cycling environment is the key point in energy harvesting process, and should be predicted by using composite modeling theories. 1-D and 3-D approach is discussed in this section to predict the stress generated. The predicted stress during phase transformation due to constrained recovery is used to generate electrical charge in piezo-phase by inverse piezoelectric effect, and later in the following sections the electrical model to estimate the available power from piezoelectric material is examined.

4.1.1. One-Dimensional Modeling

In this section piezo-SMA composite is considered as one dimensional series composite model. Both piezo electric and SMA has finite thickness and laminated together to for the energy harvesting composite. SMA used in this model is in Martensitic phase at room temperature, Fig.4.1(a), this phase is called self accommodated martensite. Prestrain is introduced to SMA by simply loading and unloading it in martensite form, Fig.4.1(b), since SMA is martensitic in room temperature SME is observed in this step and deformation in martensite proceeds by the growth of one variant at the expense of the other. Amount of the prestrain is determined by the loading stress, and here in this study it is assumed that the SMA is deformed by less then 3% strain, see schematic representation in Fig.4.2. The deformed martensitic SMA, Fig.4.1(c), is attached to piezo and the laminated composite is clamped in a way that it has zero displacement boundary condition, see Fig.4.1(d). It is expected that upon heating above the Austenite finish temperature, SMA exhibit shape memory effect and each variant reverts to the Austenitic phase in the original orientation by the reverse transformation, Fig.4.1(e). Due to fixed displacement boundary condition, where mechanical obstacle is assumed to be completely rigid and the contact strain is independent of temperature and stress; the phse transformation induced compressive stress in the composite. Both fiber and matrix will be under compression. After heating above the A_f temperature, maximum recovery stress is generated, here it is assumed that the stress generated is below the yielding stress of the SMA. The composite then cooled below the M_f temperature to finish the cycle, and the stress in the composite decreases to initial value, Fig.4.1(f).

A one-dimensional model for computing the stress in the Piezo-SMA composite generated by temperature induced martensitic and austenitic transformations is modeled by using iso-stress (constant stress) condition.

$$\sigma_c = \sigma_m = \sigma_f \tag{4.1}$$

where σ_c, σ_m and σ_f are the stress of composite, matrix and fiber respectively. Both piezo and SMA assumed to have same cross-sectional area, and f denotes the volume fraction of SMA phase in the design. During the constrained recovery, total deformation of the composite, δ_c is kept to be zero

$$\delta_c = \delta_f + \delta_m = 0 \tag{4.2}$$

where δ_m and δ_f are the deformation of matrix and fiber respectively.

Total deformation is zero since the composite is assumed to be rigidly constrained. Equation (4.2) can also be written in terms of constituents strains as

$$\varepsilon_c = f \times \varepsilon_f + (1 - f)\varepsilon_m = 0 \tag{4.3}$$

since the cross-sectional area is uniform through x_3 direction and the volume fraction of each constituent is linearly proportional to its thickness, deformation can be written as strain.

Total compressive strain for the piezo can be written as

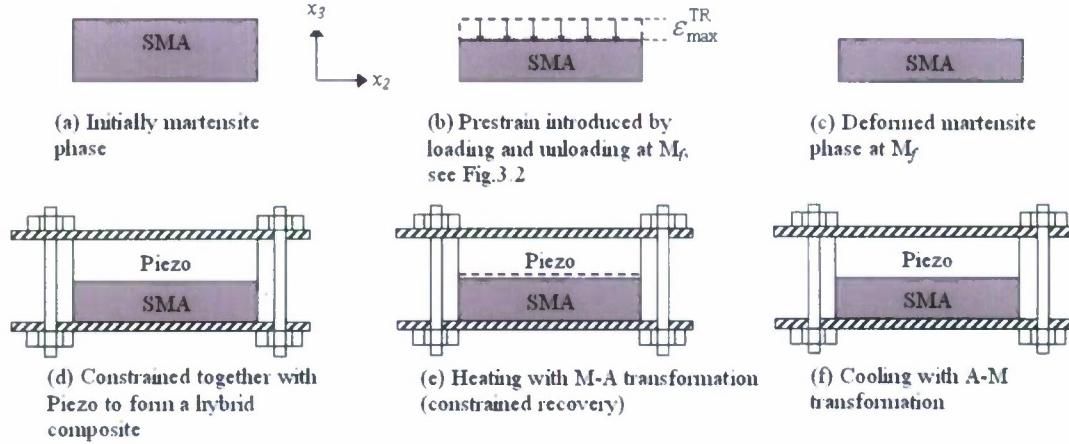$$\varepsilon_m = \varepsilon_m^{\text{TE}} - \varepsilon_m^{el} = \alpha_m \Delta T - \frac{\Delta \sigma_m}{E_m} \tag{4.4}$$

(a) Initially martensite phase

(b) Prestrain introduced by loading and unloading at M_f, see Fig.3.2

(c) Deformed martensite phase at M_f

(d) Constrained together with Piezo to form a hybrid composite

(e) Heating with M-A transformation (constrained recovery)

(f) Cooling with A-M transformation

Figure 4.1. Modeling of Piezo-SMA composite.

where $\varepsilon_m^{\text{TE}}$, α_m, ε_m^{el}, and E_m are the thermal strain, thermal expansion coefficient, elastic strain and Young's modulus of the piezo matrix. ΔT is the temperature difference between A_f and M_f, $\Delta T > 0$ for reverse (M $\rightarrow$ A) transformation, and $\Delta T < 0$ for martensitic (A $\rightarrow$ M) transformation. Total compressive strain for the SMA can be written as

$$\varepsilon_f = \varepsilon_f^{\text{TE}} + \varepsilon_f^{\text{TR}} - \varepsilon_f^{el} = \alpha_f \Delta T + \varepsilon_f^{\text{TR}} - \frac{\Delta \sigma_f}{E_f} \tag{4.5}$$

where $\varepsilon_f^{\text{TE}}$ $\varepsilon_f^{\text{TR}}$ ε_f^{el} α_f, and E_f are the thermal strain, prestrain, elastic strain, thermal expansion coefficient and the austenite phase Young's modulus of SMA fiber phase. Assuming linear dependence of $\varepsilon_f^{\text{TR}}$, E_f and α_f, see Tanaka (1986)
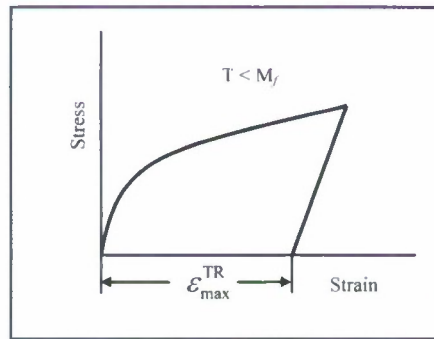

Figure 4.2. Schematic Stress-Strain curve of SMA to introduce pre-strain of amount, ε^{TR} .

$$\varepsilon_f^{TR}(\xi) = (1-\xi) \times \varepsilon_{max}^{TR} \tag{4.6}$$

$$E_f(\xi) = \xi \times E_f^M + (1-\xi)E_f^A \tag{4.7}$$

$$\alpha_f(\xi) = \xi \times \alpha_f^M + (1-\xi)\alpha_f^A \tag{4.8}$$

where E_f^M, E_f^A α_f^M, α_f^A and ξ are martensite phase Young's modulus, austenite phase Young's modulus, CTE of martensite phase, CTE of austenite phase and martensite volume fraction of fibers respectively. ξ is a function of temperature and stress. ξ can be expressed for martensitic (A → M) transformation, Mikata (2000).

$$\xi(T,\sigma)_{A \to M} = 1 - \exp\left(a^M \times (M_s - T) + b_M \times \sigma_f\right) \tag{4.9a}$$

$$a^M = \frac{\ln(0.01)}{M_s - M_f}, \ b_M = \frac{a^M}{C_M} \tag{4.9b}$$

and for reverse (M → A) transformation as

$$\xi(T,\sigma)_{M \to A} = \exp\left(a^A \times (A_s - T) + b_A \times \sigma_f\right) \tag{4.10}$$

$$a^A = \frac{\ln(0.01)}{A_s - A_f}, \ b_A = \frac{a^A}{C_A} \tag{4.11}$$

where T, σ_f, C_M, and C_A are the temperature, the effective stress of the fibers, slope of martensite transformation contour and slope of reverse transformation contour respectively. Compressive stress across the composite in the x_3-direction (along the thickness, see Fig.4.1) can be found as;

$$\Delta\sigma_c = \frac{f \times \left(\alpha_f(\xi)\Delta T + \varepsilon_f^{TR}(\xi)\right) + (1-f) \times \alpha_m \Delta T}{\left[\dfrac{f}{E_f(\xi)} + \dfrac{1-f}{E_m}\right]} \tag{4.12}$$

The stress induced by phase transformation is determined. The value of the stress is highly proportional with the transformation stress that has defined in initial steps as ε_{max}^{TR}. Further deformation in martensite phase will induced more stress in the composite that can be converted in to electrical energy by inverse piezoelectric effect. Stiffness of both piezoelectric and SMA is also another parameter that effects the amount of the stress. Stiffer the piezo the recovery stress will be higher. Stress relaxation during cooling cycle isn't calculated since it assumed that all the stress induced is heating cycle is disappears during cooling cycle due to martensitic transformation in the SMA phase, where $\xi \to 1$. One-dimensional model of energy harvester is finalized with the determination of the stress generated during the heating cycle; in the next section piezo-SMA composite will be examined by applying Eshelby's theory. The electrical model to convert mechanical energy in Electrical energy will be discussed in later sections.

4.1.2. Three-Dimensional Modeling with Eshelby Theory

A three dimensional analytical model for computing the stress and strain in the Piezo-SMA composite is examined by using Eshelby's inclusion method with Mori-Tanaka mean field theory. The schematic representation of the analytical model for the calculation of composite stress is shown in Fig.4.3 where phase transformation strain of fiber, thermal mismatch strains of fiber and matrix are shown. The composite is consists of an infinite piezoelectric matrix ($D-\Omega$) containing a finite volume fraction, f, of spheroidal SMA fillers (Ω). A deformation constraint is applied in x_3 direction for generating the recovery stress during the thermal induced phase transformation, which is represented by $\mathbf{F}^o$
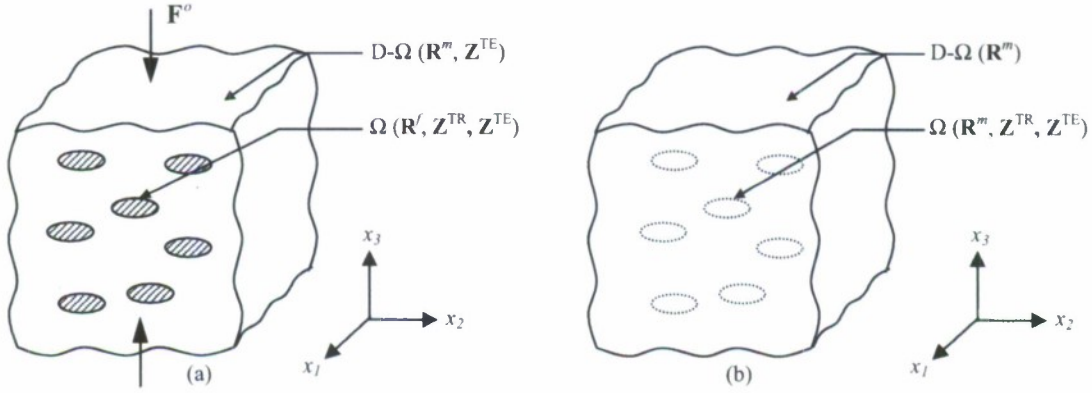
Figure 4.3. Analytical model for predicting residual stresses in SMA fiber and piezo matrix, (a) original problem is converted to (b) Eshelby's equivalent inclusion problem.

The phase transformation strain of the SMA by the shape memory effect can be expressed as

$$\mathbf{Z}^{TR} = \xi\varepsilon^{TR}\begin{bmatrix} -v_f & -v_f & 1 & 0 & 0 & 0 & 0 & 0 & 0 \end{bmatrix} = \xi\varepsilon^{TR}\mathbf{V}^{TR} \qquad (4.13)$$

where ε^{TR} and v_f denote the phase transformation strain from austenite to martensite and Poisson's ratio of the SMA, respectively. ξ is expressed for martensitic transformation and for reverse transformation in Eqs.(4.9) and (4.10).The thermal mismatch strain is generated during the cooling and heating processes due to difference in CTEs of the SMA and PZT, and it is expressed as

$$\mathbf{Z}^{TE} = \alpha^\Delta\begin{bmatrix} 1 & 1 & 1 & 0 & 0 & 0 & 0 & 0 & 0 \end{bmatrix} = \alpha^\Delta\mathbf{V}^{TE} \qquad (4.14)$$

where $\alpha^\Delta = (\alpha_f - \alpha_m)\Delta T$, and α_f, α_m and ΔT are the CTEs of the fiber and matrix, and temperature change, respectively. Both Austenite and martensite phase have different CTEs, α_f which can be assumed to be linear function of ξ during the phase transformation, Tanaka (1986).

By using Eshelby's inclusion method with Mori-Tanaka interaction effect, the stress distribution for SMA phase can be expressed as

$$\Sigma^f = \mathbf{R}^f \cdot \left(\overline{\mathbf{Z}} + \mathbf{Z} - \mathbf{Z}^{TE} - \mathbf{Z}^{TR}\right) \qquad (4.15)$$

$$\Sigma^f = \mathbf{R}^m \cdot \left(\overline{\mathbf{Z}} + \mathbf{Z} - \mathbf{Z}^*\right) \qquad (4.16)$$

where $\mathbf{R}$ is the electro-elastic stiffness matrix, $\mathbf{Z}$ is the field vector, $\overline{\mathbf{Z}}$ is the average elastic field in the matrix domain, $\mathbf{Z}^*$ is the equivalent eigenfield of the equivalent inclusion, and superscripts f and m refer to the fiber and matrix, respectively. Electro-elastic stiffness of fiber $\mathbf{R}^f$ depends on ξ and is assumed to be a linear function of ξ Tanaka (1986). Therefore electro-elastic stiffness matrix for SMA phase can be written as

$$\mathbf{R}^f = \xi \times \mathbf{R}^f_M + (1 - \xi)\mathbf{R}^f_A \tag{4.17}$$

where $\mathbf{R}^f_M$ and $\mathbf{R}^f_A$ are the electro-elastic stiffness of martensite and austenite phase of SMA respectively.

The integration of the disturbance stress σ_{ij} over the entire domain (D) vanishes, average field disturbance in the matrix can be written as

$$\overline{\mathbf{Z}} = -f\left(\mathbf{Z} - \mathbf{Z}^*\right) \tag{4.18}$$

The total strain field $\mathbf{Z}$ and $\mathbf{Z}^*$ are related through

$$\mathbf{Z} = \mathbf{S} \cdot \mathbf{Z}^* \tag{4.19}$$

where $\mathbf{S}$ is the coupled electro-elastic analog of Eshelby's tensor as defined by equation given in Mikata (2000) where $\beta \to \infty$ for elliptic crack like inclusions normal to x_3-direction in transversely isotropic piezoelectric matrix. For a flat oblate spheroid (penny-shaped) inclusion embedded in a transversely isotropic piezoelectric matrix, Eshelby tensor is given by 9 by 9 matrix, see Taya (2005).

Rewrite equation (4.22) by plugging (4.24) and (4.25) in terms of $\mathbf{Z}^*$

$$\boldsymbol{\Sigma}^f = (1 - f)\mathbf{R}^m \cdot (\mathbf{S} - \mathbf{I}) \cdot \mathbf{Z}^* \tag{4.20}$$

In order to define eigenstrain, $\mathbf{Z}^*$ one can equate Eqs.(4.15) and (4.16) and plug (4.19) to get,

$$\mathbf{Z}^* = \left[(1 - f)\left(\mathbf{R}^f - \mathbf{R}^m\right) \cdot \mathbf{S} + \mathbf{R}^m + f\left(\mathbf{R}^f - \mathbf{R}^m\right)\right]^{-1} \cdot \mathbf{R}^f \cdot (\mathbf{Z}^{TE} + \mathbf{Z}^{TR}) \tag{4.21}$$

Equation (4.21) can be used in (4.20) to determine the flux vector

$$\boldsymbol{\Sigma}^f = (1 - f)\mathbf{R}^m \cdot (\mathbf{S} - \mathbf{I}) \cdot \left[(1 - f)\left(\mathbf{R}^f - \mathbf{R}^m\right) \cdot \mathbf{S} + \mathbf{R}^m + f\left(\mathbf{R}^f - \mathbf{R}^m\right)\right]^{-1} \cdot \mathbf{R}^f \cdot (\mathbf{Z}^{TE} + \mathbf{Z}^{TR}) \tag{4.22}$$

The average flux vector in the fiber, $< \boldsymbol{\Sigma}^f >$ can be computed as

$$< \boldsymbol{\Sigma}^f > = \mathbf{RE} \cdot (\mathbf{Z}^{TE} + \mathbf{Z}^{TR}) \tag{4.23}$$

Since internal flux field over the entire composite domain vanishes, for matrix average flux vector,

$$< \boldsymbol{\Sigma}^m > = \frac{f}{f - 1}\mathbf{RE} \cdot (\mathbf{Z}^{TE} + \mathbf{Z}^{TR}) \tag{4.24}$$

where

$$\mathbf{RE} = (1 - f)\mathbf{R}^m \cdot (\mathbf{S} - \mathbf{I}) \cdot \mathbf{A} \cdot \mathbf{R}^f \tag{4.25}$$

$$A = \left[(1 - f)(R^f - R^m) \cdot S + R^m + f(R^f - R^m) \right]^{-1} \tag{4.26}$$

It is noted that bold face, RE, R^i and A are 9 by 9 matrices.

Field tensor in matrix domain can be written as

$$Z^m = F^m < \Sigma^m > \tag{4.27}$$

where the material properties of matrix are used in determining the compliance property tensor, F^m.

Stress generated during the reverse transformation of the SMA is predicted with using two approaches; one-dimensional model, and 3D model with Eshelby's theory. Material properties and characterization of SMA will be discussed in the following section. Electrical model will be introduced in the following section to characterize the Piezo material used in thermal energy harvester in the following sections.

4.2. Shape Memory Alloy (SMA) Characterization

In a shape memory alloy (SMA), the shape memory effect (SME) and super-elasticity (SE) or transformation pseudo-elasticity appear and are dependent on stress and temperature. In nitinol (NiTi) SMA, SME and SE appear due to the martensitic transformation (MT) and the rhombohedral phase transformation (RPT), Miyazaki (1984 and 1986), and Otsuka (1990). In applications to an actuator, a robot and a solid state heat engine, a SMA is used as a working element which performs cyclic motions. The working characteristics of the SMA element are specified by the beginning and completion temperatures of the motion, the working stroke and the working force. These characteristic values are determined by the transformation temperature, the transformation strain and the transformation stress of the material.

In this section of the study material properties of SMA are examined. The experimental equipments used to characterize the Shape memory behavior includes Differential Scanning calorimeter (DSC), and Instron Mechanical Testing (MT) machine. DSC is used to determine the temperatures associated with phase transformation with in the SMA. Compression testing is performed with mechanical testing device to examine the SME of the material.

The material which is used in Piezo-SMA energy harvester modeling is a 51.2Ti-48.8Ni (at.%) SMA. The geometry can be described as a disc shape. The transformation temperatures determined by using DSC were as follows: $M_s=313°K$, $M_f=293°K$, $A_s=328°K$ and $A_f=343°K$, as can be seen from Fig.4.4, note the temperature values are in °C in DSC results. Hysteresis in transformation is about 50K.

The peak in cooling curve, Fig.4.4, is called martensitic, $B2 \rightarrow B19'$ transformation, the starting and ending temperature values corresponds the martensitic starting temperature, M_s and martensitic finish temperature, M_f respectively. This helps to find the critical temperatures for the SMA that is used in experimental study.

It is experienced from the study that Ni-content, aging, thermo-mechanical treatment and additional of alloying elements, are important for controlling the memory behavior, in other words one can change the critical transformation temperatures by simple changing the Ti content in the NiTi alloy.
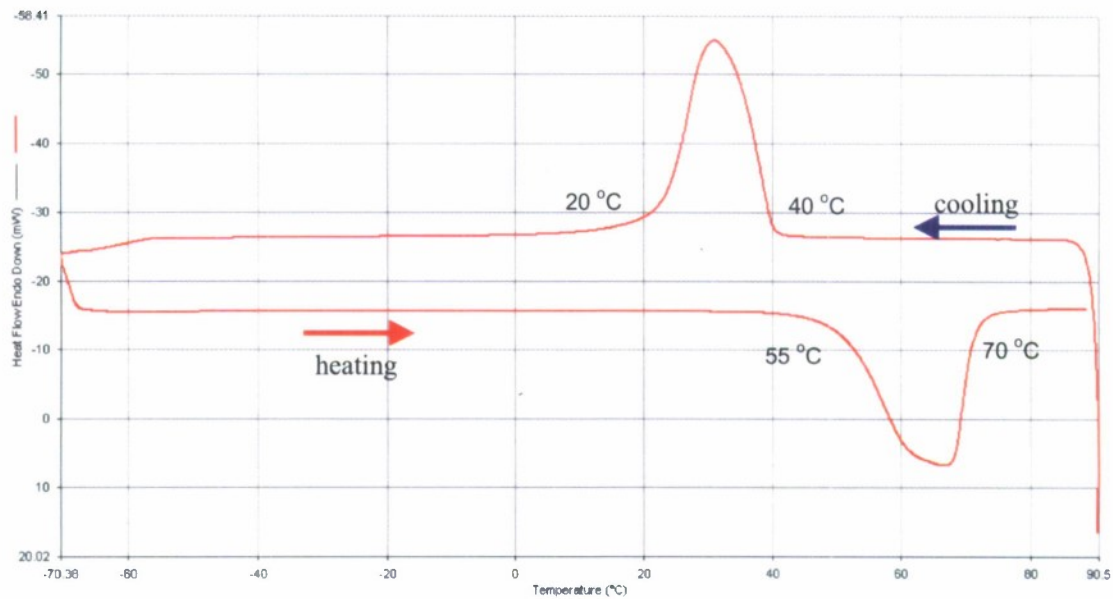
Figure 4.4. DSC result of 51.2Ti-Ni (at.%) SMA.

The stress-strain properties of the SME were examined for the SMA material, see Fig.4.5. At first, the loading and unloading processes with maximum strain ε_{max}^{TR} were performed at a low temperature T_L below martensite finish temperature, M_f. While maintaining zero load, by simple using the load control option of Testing device, the sample was heated to high temperature T_H above Austenite finish temperature, A_f and the process is followed by cooling to T_L.

Starting material for SMA phase used in energy harvester is deformed (twinned) martensite as discussed before; therefore the pre-strain introduced by compressive stress is a key parameter to be measured before going to further steps in the experimental study. Defining the pre-strain is performed simply by using the Stress-Strain curve generated by compressive testing followed by heating above A_f temperature.
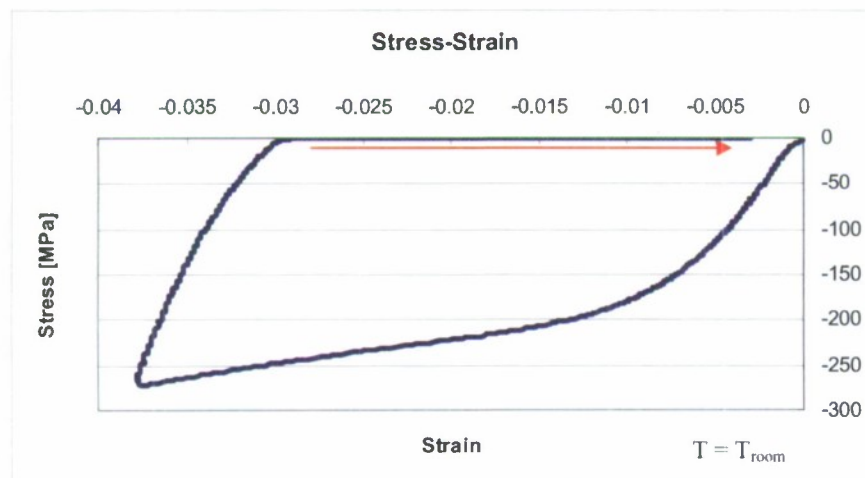
Figure 4.5. Stress-Strain response of 51.2Ti-48.8Ni (at.%) SMA, at Room Temperature

After several testing the case that can be seen in Fig.4.5 is selected to be used in defining the starting properties of the SMA used in Experimental study and analytical modeling. Approximately 2.5% compressive strain is introduced to NiTi material, as it can be seen from the chart most of the strain can be recovered by Shape Memory effect simply by heating above the A_f temperature.

Experiments in order to characterize the material properties of SMA yield the design variables such as critical temperatures in phase transformations, pre-strain that is introduced by simply loading and unloading the SMA at a temperature below then Martensite finish temperature and other mechanical properties such as Martensitic and Austenitic Young's modulus. With all parameters, 1D model and 3D model with Eshelby's theory, the stress generation in the composite, especially in piezoelectric material phase, is predicted. The results are shown in Fig.4.6 for 1D model and Fig.4.7 for 3D model respectively. From both 1D and 3D result one can tell that during heating when A_s is reached, reverse transformation starts and small amount of transformation strain, $\delta\varepsilon_{TR}$ is recovered and causes the compressive stress to induce. Then the reverse transformation is suppressed. If the temperature wouldn't be increasing at this point the recovery stress generation would have been stopped, however temperature increases and this increase induces further transformation. Eventually when the temperature at which maximum recovery stress has reached; reverse transformation is completed.
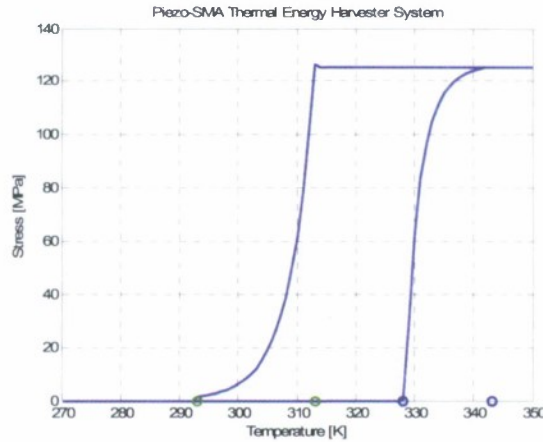

Figure 4.6. Effective piezo stress based on 1-D model as a function of temperature.

During cooling when M_S is reached, forward transformation starts, compressive stress reduces by an amount of $\delta\varepsilon_{TR}$ and forward transformation suppressed. To induce further forward transformation, temperature is decreased. Eventually when the compressive stress is totally released complete forward transformation occurs.
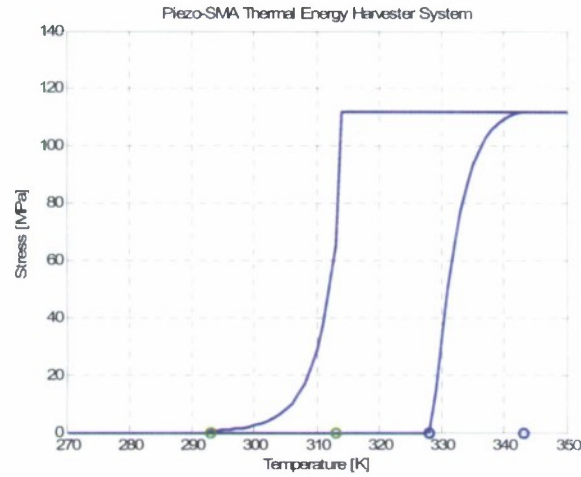
Figure 4.7. Effective piezo stress based on 3-D model with Eshelby's Theory as a function of temperature.

With the material properties and Thermal boundary conditions, ie heating above the A_f followed by cooling below M_s temperature, the stress generated during constrained recovery in piezoelectric phase, x_3-direction, calculated as ~125 MPa with 1D model and ~110 MPa with 3D Model with Eshelby's Theory. It is noted that in both even tough it has been modeled in the analytical mode, thermal expansion is neglected in predicting the results.

Martensite volume fraction of the SMA phase is exponentially related to temperature and effective stress in SMA phase within the composite, as formulated in Eqs.(4.15, 4.16). For the numerical computation of the effective matrix stress the martensite volume fraction with respect to temperature is also plotted as in Fig. 4.8.
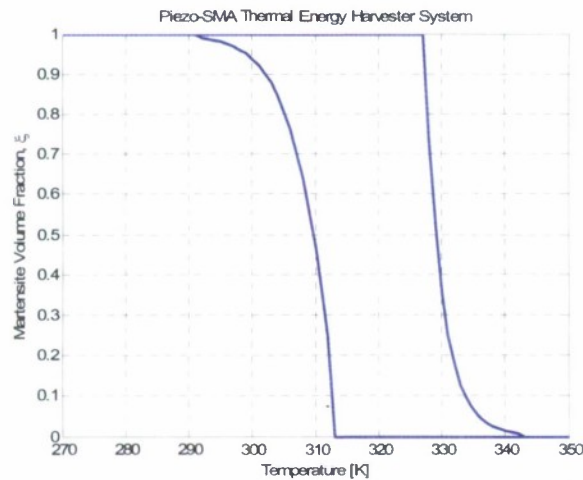

Figure 4.8. Martensite volume fraction of the piezo-SMA hybrid composite during thermal cyeling based on 3-D model with Eshelby's Theory

4.3. Electrical Model

It is convenient to develop analytical models that can predict the response of these piezoelectric elements under different input conditions and for various material properties. It is known that piezoelectric material constants are not constants at all as they depend in a nonlinear fashion on conditions such as mechanical and electrical boundary conditions, and the frequency and amplitude of the excitation force profile. These effects must be considered when using this model to predict piezoelectric response under conditions significantly different from those for which the model parameters are determined.

The piezoelectric material also has a considerable impact on achievable performance of the transducer. Commonly used piezoelectric materials are based on lead zirconate titanate (PZT) ceramics. Assuming that a PZT disk is directly used as a transducer, the significant material parameters can be outlined to provide the material figure of merit. There are many factors that influence the selection of the PZT composition. The constitutive equations for a linear piezoelectric material under low stress levels can be written as;

$$\varepsilon_{ij} = s_{ijkl}\sigma_{kl} + g_{kij}D_k \tag{4.28}$$

$$-E_i = g_{ijk}\sigma_{jk} - \beta_{ij}D_i \tag{4.29}$$

where σ is the strain, D is the electric displacement, E is the electric field, s is the elastic compliance, and g is the piezoelectric voltage coefficient given as

$$g = \frac{d}{\kappa_o\kappa} \tag{4.30}$$

here, d is the piezoelectric constant and κ is the dielectric constant. The constant β in Eq.(4.29) is the dielectric susceptibility, and equal to the inverse dielectric permittivity tensor component. Under applied force $F = \sigma \cdot A$ (where A is the area), the open circuit output voltage (V) of the piezoelectric material can be computed from Eq.(4.29), and given as;

$$V = E \cdot t = -g \cdot \sigma \cdot t = -\frac{g \cdot F \cdot t}{A} \tag{4.31}$$

where t is the thickness of the piezoelectric material. The charge (Q) generated on the piezoelectric can be determined from Eq.(4.28) and given as;

$$D = \frac{Q}{A} = \frac{E}{\beta} = \frac{V \cdot \kappa_o\kappa}{t} \tag{4.32}$$

or

$$Q/V = \frac{\kappa_o\kappa \cdot A}{t} = C \tag{4.33}$$

where C is the capacitance of the piezo material. The above relationship shows that at low frequencies a piezoelectric plate can be assumed to behave like a parallel plate capacitor. Hence, electric power available under the cyclic excitation with frequency, f, is given as follows;

$$P = \frac{1}{2}CV^2 \cdot f \tag{4.34}$$

35

or

$$P = \frac{1}{2} \frac{d^2}{\kappa_o \kappa} \cdot F^2 \cdot \frac{t}{A} \cdot f \qquad (4.35)$$

Under certain experimental conditions, for a given material of fixed area and thickness, the electrical power is dependent on the d^2/κ ratio of the material. A material with a high d^2/κ ratio will generate high power when the piezoelectric ceramic is directly employed for harvesting energy.

4.4. Experimental Study

Modeling of piezo-SMA composite as a thermal energy harvester material has been discussed in previous sections, here design specifications are summarized based on modeling and material properties. Prediction of the experimental condition is done based on simple one dimensional model. The material properties used in experimental study is shown in Table 4.1. These properties are used in 1D modeling to predict stress in piezo phase and the power available to electrical loading which will be discussed in later sections.

Table 4.1. Material Properties of PZT and SMA

Young's Modulus [GPa]	PZT: E_{11}: 59, E_{33}: 51 SMA: $E_{Austenite}$: 67, $E_{Martensite}$: 26.3
Piezoelectric Voltage Constant [10^{-3} Vm/N]	$g_{33} = 21$, $g_{31} = -9$, $g_{33} = 27$
Piezo Thickness, h [mm]	1
Piezo Area [m^2]	2.5×10^{-4}
Capacitance, C [nF]	19.5
Frequency, f [Hz]	0.01

One-Dimensional serial model is used to predict stress generated during thermal cycling process of the composite. By neglecting the thermal expansion term in Eq.(4.12) the stress equation reduces to;

$$\Delta\sigma = \frac{\varepsilon_f^{TR}(\xi)}{\left[\dfrac{f}{E_f(\xi)} + \dfrac{1-f}{E_m}\right]} \tag{4.36}$$

As martensite volume fraction $\xi \to 0$, the stiffness of the SMA phase approaches the Austenite stiffness as expected, $E_f(\xi) \to E_f^A$.

With volume fraction $f = 0.1$ and pre-strain, as Shown in Fig.4.5, $\varepsilon_f^{TR}(\xi) = 0.025$, the stress change is calculated as approximately 120 MPa.

The material dimensions for SMA are given as; diameter 4.6 mm, and thickness is 2.7 mm; the force exerted on PZT can be calculated as;

$$F = \Delta\sigma \cdot A = (120)(\pi\, d_.^2\, /4) = 2\,\text{kN} \tag{4.37}$$

Now that the force is predicted by using one dimensional model the response of PZT for the same loading condition with different frequencies are experimentally measured in order to find the power available to electrical load.

The voltage can be calculated by inverse piezoelectricity, Eq.(4.31), and it is found to be ~200 Volt with the given material properties, See Table 4.1 and the predicted load from, Eq.(4.37). By assuming as low frequencies the PZT behaves like a parallel plate capacitor, power available from PZT can be calculated for the known excitation frequency, f.

Here the concept of impedance matching is also convenient to discuss; in electrical engineering, the maximum power transfer theorem states that to obtain maximum external power from a source with a finite internal impedance, the impedance of the load must be made as same as that of the source. Therefore the power equation for the electrical load, P_L connected to PZT source can be derived by using the simple circuit shown in Fig.4.9.
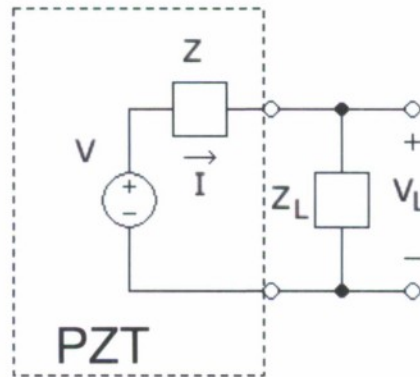

Figure 4.9. Schematic representation of PZT connected to electrical loading

The current, I, can be written as;

$$I = \frac{V}{Z + Z_L} \tag{4.38}$$

and the voltage, V_L, over the electrical load Z_L;

$$V_L = V \frac{Z_L}{Z_L + Z}$$ (4.39)

the maximum power transfer theorem states that $Z_L = Z$, then power at electrical load can be calculated from $P_L = I \cdot V_L$

$$P_L = \left[\frac{V}{Z + Z_L} \right] \cdot \left[V \frac{Z_L}{Z_L + Z} \right]\bigg|_{Z = Z_L} = \left[\frac{1}{4} \right] \frac{V^2}{Z}$$ (4.40a)

Open circuit power, P, for piezoelectric material is predicted with Eq.(4.34) or Eq.(4.35),

$$P_L = \left[\frac{1}{4} \right] \frac{V^2}{Z} = \left[\frac{1}{4} \right] \frac{1}{2} C V^2 \cdot \mathrm{f}$$ (4.40b)

Equations (4.40) relates the power at electrical load to Power available from PZT material, and it shows that only ¼ of the power is available for electrical loading. This information is very important before going in to further steps in experimental study where the impedance of the piezoelectric material will be determined at different frequencies with different electrical loading conditions; in order to find impedance of the piezoelectric system and the maximum power available to electrical load.

4.5. Piezoelectric Material (PZT) Characterization

In order to determine the power available to electrical load from the PZT material in the piezo-SMA thermal energy harvester some sets of experiments are carried out with different frequencies. For each case fixed frequency, different load resistance are connected to PZT material which is under cyclic mechanical loading in order to determine the best impedance for the PZT material that is used in thermal energy harvesting design. The schematic representation of the electrical circuit used in these set of experiments are shown in Fig.4.9. Here it is modeled that PZT behaves as a voltage generator with has an internal impedance of Z and the electrical load Z_L is connected to output of the PZT material. The voltage over electrical load is monitored with DAQ.
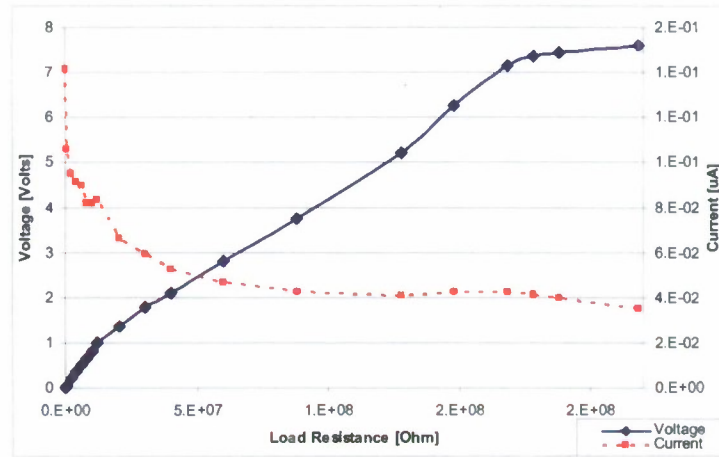
Figure 4.10. Voltage and Current response for 0.01 Hz, 2kN loading

Figures 4.10 and 4.11 summarize the experiments performed by loading condition, 2kN at 0.01Hz. In this experiment piezoelectric material is subjected to cyclic loading with mechanical testing device, loading is compressive all time which is varying from 0 to 2kN. Load resistance is increased and the experiment performed with the same condition till the voltage across the load resistance is saturated the voltage and current is plotted versus load resistance as can be seen in Fig.4.10, and the power available to electrical load is shown in Fig. 4.11.
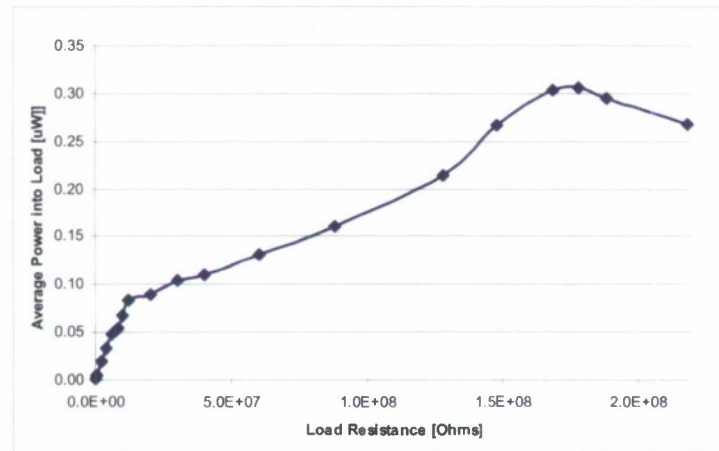
Figure 4.11. Average power at the electrical load for different electrical loading 0.01 Hz, 2kN

As it can be seen from Fig.4.10, the maximum average power at the electrical load can be found at electrical load of ~180 MΩ where the voltage is measured to be ~7.4 Volts, and the current over the resistance, calculated by Ohm's Law, is 0.042 μA. The average power is measured as

$$P_L^m = V_L^m \cdot I_L^m = 0.31 \ \mu W. \tag{4.41}$$

where superscript "m" represents the values are measured.

Recall Eq.(4.40) which relates the power at electrical load to Power available from PZT material with known excitation frequency, which is 0.01 Hz;

$$P_L = \left[\frac{1}{4}\right]\frac{V^2}{Z} = \left[\frac{1}{4}\right]\frac{1}{2}CV^2 \cdot f = 0.95 \ \mu W \tag{4.42}$$

By comparing the results in (4.41) and (4.42) it is convenient to say that the analytical approach by predicting the stress and the power available at electrical loading is not predicting the power available at electrical load accurately. This is mainly because of the internal loss due to low frequency excitation which is not considered in the analytical model.

In the 0.01 Hz 2 kN experiments the impedance of the PZT from maximum load transfer theorem is found to be 180 MΩ, which is relatively high in order to build an electrical circuit to store the available power from the energy harvesting composite.
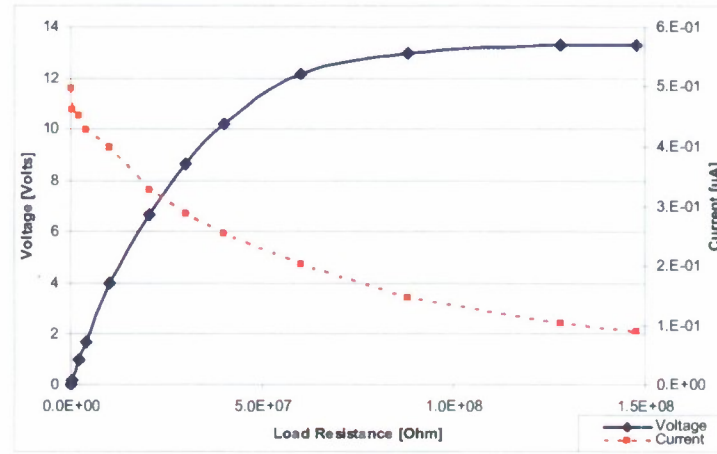

Figure 4.12. Voltage and Current response for 0.05 Hz, 2kN loading

The frequency is a key variable in the power calculation as discussed previous sections, in order to see the effect of frequency to the average power available at the electrical load, PZT experiment is carried out with different frequency conditions; the second set of the experiments performed with 0.05 Hz, 2kN loading condition. The results are summarized in Figs.4.12 and 4.13. With an increase of 5 times in the frequency the maximum power available at electrical load is measured to be ~2.6 μW.

At low values of resistance no voltage is produced (short circuit) and no power is generated. At high resistances (open circuit) no current flows and no power is generated. As the input frequency increases, the maximum efficiency occurs at smaller load resistance values. This is the behavior expected for an essentially capacitive device; as the excitation frequency increases, the source impedance $Z = 1/j\omega C$ will decreases. Therefore by assuming the capacitance is not changing during the process the expected internal impendence at 0.05 Hz is expected to be 5 times smaller then the internal impedance determined for 0.01 Hz case. By checking the maximum power transfer theorem for 0.05 Hz, the internal resistance is found to be 40 MΩ, which is 4.5 times smaller than the load value found in 0.01 Hz experiment with maximum power theorem. Analytical model shows a reasonable agreement with experimental results in this manner.
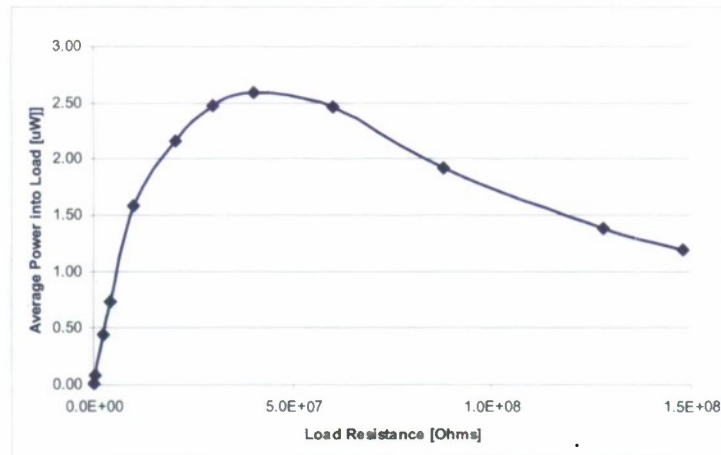
Figure 4.13. Average power at the electrical load for different electrical loading 0.05 Hz, 2kN

As it can be seen from Fig.4.13, the maximum average power at the electrical load can be found at electrical load of ~40 MΩ where the voltage is measured to be ~10.2 Volts, and the current over the resistance, calculated by Ohm's Law, is 0.26 μA. The average power is measured as

$$P_L^m = V_L^m \cdot I_L^m = 2.6 \ \mu W. \tag{4.43}$$

where superscript "m" represents the values are measured.

Recall Equation (4.44) which relates the power at electrical load to Power available from PZT material with known excitation frequency, which is 0.05 Hz;

$$P_L = \left[\frac{1}{4}\right]\frac{V^2}{Z} = \left[\frac{1}{4}\right]\frac{1}{2}CV^2 \cdot f = 4.75 \ \mu W \tag{4.44}$$

Again the analytical prediction for power available at electrical load over predicts the value for 0.05 Hz case.

The third set of the experiments performed with 0.1 Hz, 2kN loading condition. The results are summarized in Figs.4.14 and 4.15. With an increase of 2 times in the frequency the maximum power available at electrical load is measured to be ~6.4 μW.
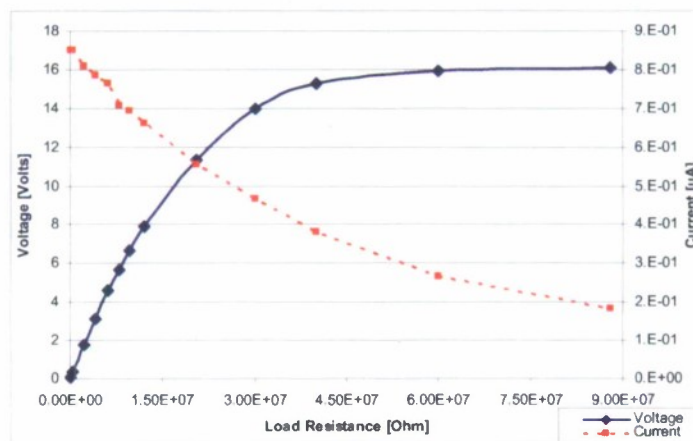

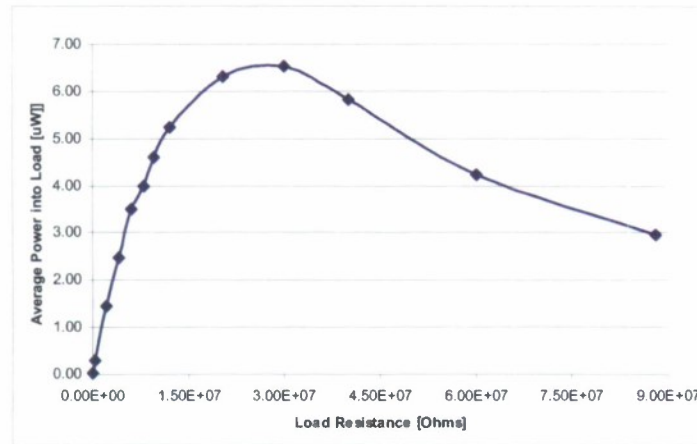Figure 4.14. Voltage and Current response for 0.1 Hz, 2kN loading

41

Figure 4.15. Average power at the electrical load for different electrical loading 0.1 Hz, 2kN

As it can be seen from Fig.4.15, the maximum average power at the electrical load can be found at electrical load of ~22 MΩ where the voltage is measured to be ~13 Volts, and the current over the resistance, calculated by Ohm's Law, is 0.52 μA. The average power is measured as

$$P_L^m = V_L^m \cdot I_L^m = 6.4 \ \mu W. \tag{4.45}$$

where superscript "m" represents the values are measured.

Recall Equation (4.44) which relates the power at electrical load to Power available from PZT material with known excitation frequency, which is 0.1 Hz;

$$P_L = \left[\frac{1}{4}\right]\frac{V^2}{Z} = \left[\frac{1}{4}\right]\frac{1}{2}CV^2 \cdot f = 9.5 \ \mu W \tag{4.46}$$

Again the analytical prediction for power available at electrical load over predicts the value for 0.1 Hz case. It can be noted that the increase in frequency leads the prediction in better agreement; this is mainly because internal loss is relatively getting smaller.

The fourth set of the experiments performed with 0.5 Hz, 2kN loading condition. The results are summarized in Figs.4.16 and 4.17. With an increase of 5 times in the frequency with respect to third experiment the maximum power available at electrical load is measured to be ~ 45 μW.
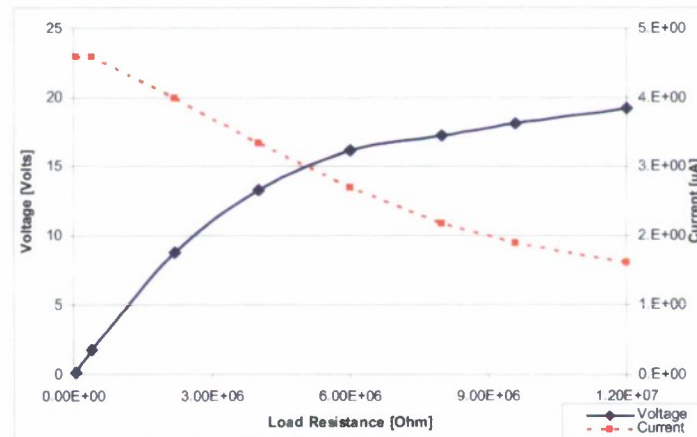

Figure 4.16. Voltage and Current response for 0.5 Hz, 2kN loading

As it can be seen from Fig.4.17, the maximum average power at the electrical load can be found at electrical load of ~ 4 MΩ where the voltage is measured to be ~13 Volts, and the current over the resistance, calculated by Ohm's Law, is 3.3 μA. The average power is measured as

$$P_L^m = V_L^m \cdot I_L^m = 45 \ \mu\text{W}. \tag{4.47}$$

where superscript "m" represents the values are measured.

Recall Eq.(4.40) which relates the power at electrical load to Power available from PZT material with known excitation frequency, which is 0.5 Hz;

$$P_L = \left[\frac{1}{4}\right]\frac{V^2}{Z} = \left[\frac{1}{4}\right]\frac{1}{2}CV^2 \cdot \text{f} = 47.5 \ \mu\text{W} \tag{4.48}$$

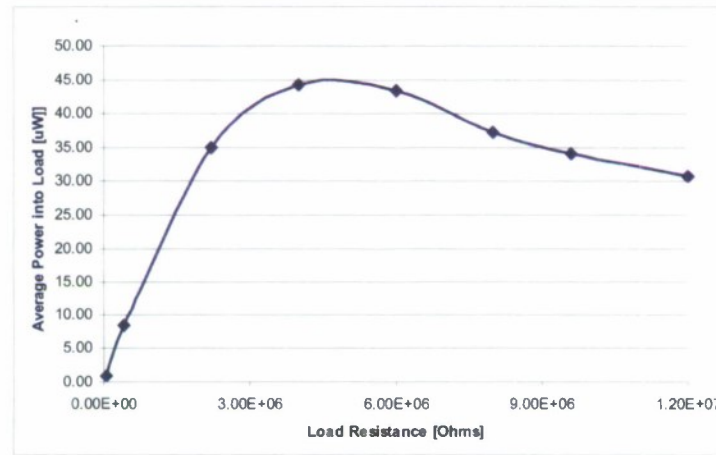Analytical prediction for power available at electrical load well predicts the value for 0.5 Hz case.

Figure 4.17. Average power at the electrical load for different electrical loading 0.5 Hz, 2kN

All four experimental conditions which are at different excitation frequencies are summarized in Fig.4.17. Logarithmic scale is used to show all data in the same plot. As it can be seen higher the frequency the power available at the electrical load is higher. The impedance at the higher frequencies is also lower then the impedance values for lower frequencies. This study with piezoelectric material gives an idea about the internal impedance of the piezoelectric material, in other words parameter identification of piezoelectric material is done by doing cyclic loading experiments with different frequencies and different load resistance. It can be noted again here that maximum power available at electric load when the impedance of the piezoelectric material matches with the connected load resistance.
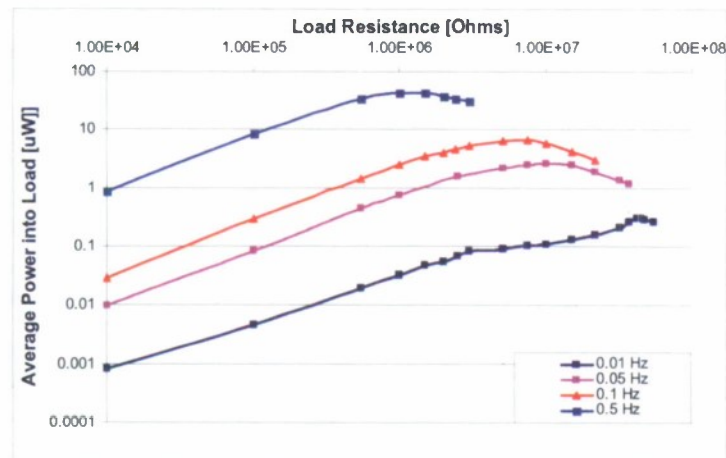
Figure 4.18. Average power at the electrical load for all frequency conditions in logarithmic scale, with respect to load resistance
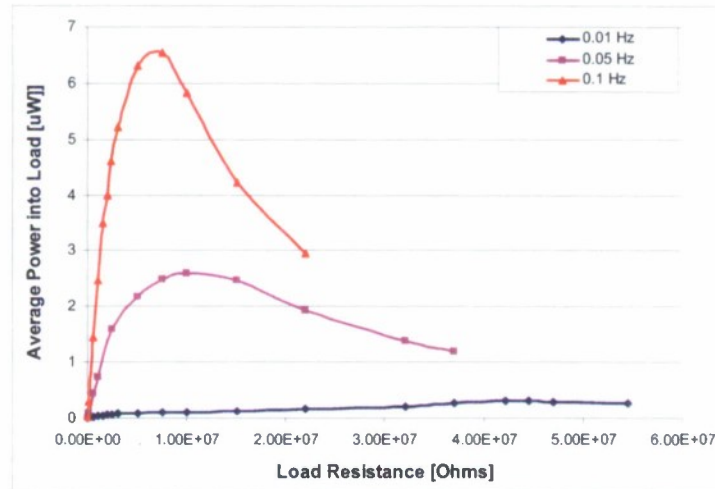

Figure 4.19. Average power at the electrical load for small frequency conditions with respect to load resistance

Figure 4.19 show the smaller frequencies; 0.01 Hz, 0.05 Hz and 0.1 for cyclic loading condition. This figure is not in logarithmic scale to give the reader better understanding of the relation between maximum power available at electrical load with respect to load resistance.

4.6. Experimental Procedure and Results

Now that the modeling and parameter identification for materials that is used in the experimental study is discussed, we shall examine the experimental procedure that is done in order to simulate temperature cycling. Figure 4.20 shows the setup of the piezo-SMA module, two piece of PZT is used in the setup in order to prevent short circuit event in the electrical schema, positive poled are attached together, and the negative poles are connected via single electrode. With this simplification the use of a separate insulation material is no more necessary. Ni-51.2% Ti is used for SMA material, the transformation temperatures are given in Fig.4.4.
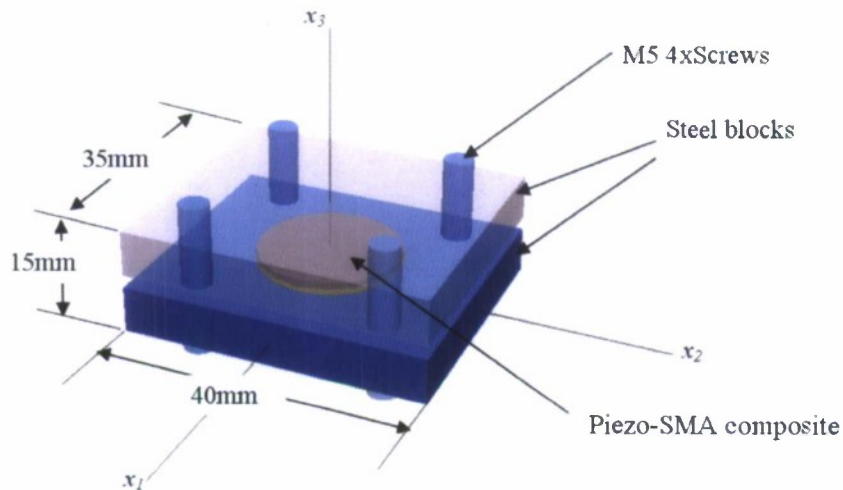
Figure 4.20. Schematic representation of the Piezo-SMA composite module in thermal energy harvesting experiment

In Fig.4.21 the setup for temperature cycle is shown. Two different temperature environments are prepared according to the SMA's transformation temperature. Hot environment is controlled by simply on-off type thermostat; the temperature is set to be higher then the Austenite finish temperature. Cold bath is prepared with accordingly Martensite finish temperature. The specimen prepares as shown in Fig.4.20 is subjected to hot and cold environments, surface temperature of the SMA specimen is monitored with a thermocouple attached on the surface. Output voltage of the PZT is monitored by Data Acquisition System (DAQ). Electrical connection is prepared with respect to Fig.4.9 where Z_L is just a know resistance element. The resistance value of electrical load is determined with respect to experimental study that is performed with piezoelectric material. The value of electrical load at which the maximum power is reach at the load is used for the experimental study performed in Thermal cycling simulations. Two PZTs are used in the composite which are serially connected with positive electrodes are touching each other, and the negative electrodes are in contact with SMA and the fixture. This creates self electrical insulation for the experimental set-up.
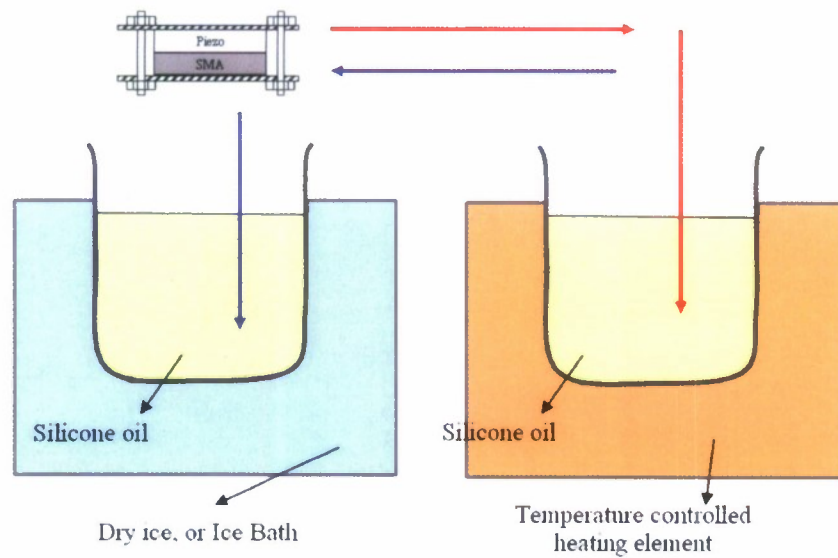
Figure 4.21. Temperature Cycle simulation for piezo-SMA Thermal energy harvester

Figure 4.22 shows the output results of the thermal cycling experiment of Piezo-SMA composite as an energy harvester. PZT module's electrodes are connected to DAQ system directly, which is not an accurate way to measure the voltage generated by the PZT material in general as we discussed earlier, the load resistance that is determined from impedance matching should have been used in this experiment. However this method provides a way to monitor the charge generated during heating and cooling periods of the thermal cycling process. As expected a positive voltage is generated during heating; SMA constrained recovery suppresses compressive stress in the system. Compressive stress on the PZT causes a positive charge accumulation. Poling direction of the PZT is also x_3-direction which is the same direction of applied force due to compressive stress, therefore d_{33} effect takes place in heating process. Cooling on the other hand cause SMA to have martensitic transformation and the compressive stress is released in the system. The rate of change in the loading on PZT is opposite to poling direction and negative voltage generated.
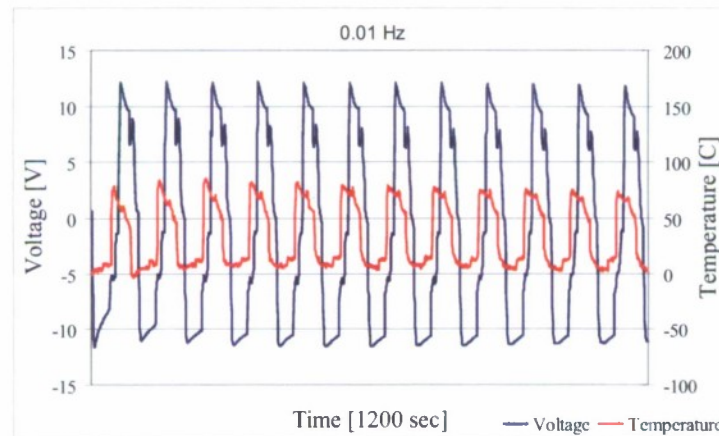

Figure 4.22. Output voltage and Temperature results for Thermal Cycling process, 0.01 Hz

Temperature is monitored by a thermocouple attached to the surface of the SMA. Monitoring the surface temperature is one of the solutions in order to check the if the material is subjected a thermal cycle between critical transformation temperatures; it this case Martensite finish M_f and Austenite finish A_f temperatures which are predetermined by DSC test as shown in Fig.4.4.
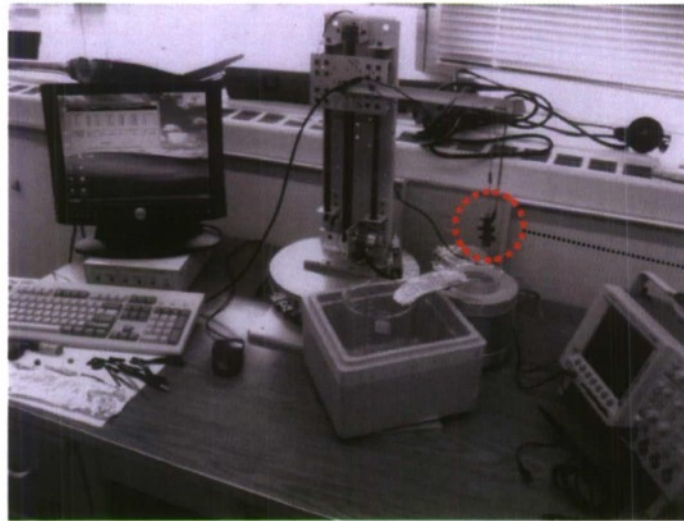

Figure 4.23. Experimental setup, piezo-SMA composite is subjected to thermal cycling

Experimental setup can be seen in Fig.4.23, thermal energy harvester, shown in circle is dipped in to hot and cold baths with the help of a robotic arm, as schematically represented in Fig.4.21. The robotic arm is driven by an open loop control system, the duration and the position can be determined accordingly by just changing the speed of the arm to simulate the thermal cycling process.

Cold and Hot baths are placed next to each other in order to minimize the temperature variation during robotic arms travel between the positions. The traveling time is minimized in order to have a better simulation. It is convenient to say that all the inertial effects limit the optimization of the temperature fluctuation.

Second sets of experiment is carried out with Instron Mechanical testing machine, same piezo-SMA composite is clamped with the help of compression punch of testing machine, and the controlled is switched to position control in order to have zero displacement boundary condition. The heating and cooling is applied to the SMA. The temperature is measured with a thermocouple which is inserted 3mm inside the SMA material from the free side. Piezoelectric material is connected to a known electrical load of 40 MΩ; this resistance is selected since the parameter identification experiments for piezoelectric material suggested using 40 MΩ of electrical load to have maximum power available for the load itself, see Fig.4.13.
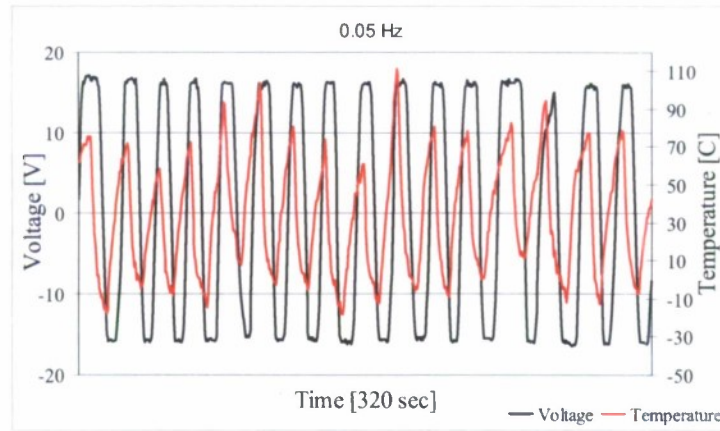
Figure 4.24. Output voltage and Temperature results for Thermal Cycling process, 0.05 Hz

Voltage across the electrical load and the temperature response in the SMA is plotted as can be seen in Fig.4.24. The RMS value of voltage is 12.1 Volt. The average power is measured as

$$P_L^m = V^2\big/R = 3.6 \ \mu W. \tag{4.49}$$

The result can be compared with two previously examined cases; analytical model to estimate the power available and results from parameter identification experiments performed with the same frequency. Overall study is summarized in the Table 4.2. Where the predicted power is based on Eq.4.40 and the measured values are recorded from piezoelectric material's parameter identification experiments and thermal fluctuation experiment performed with cold and hot bath/stream.

Table 4.2. Prediction and Experimental results for power available at electrical load

Frequency [Hz]	Predicted Power [uW]	Power Measured with Piezo only Experiments [uW]	Power Measured with Thermal fluctuation [uW]
0.01	0.95	0.31	*
0.05	4.75	2.6	3.6
0.1	9.5	6.5	N/A
0.5	47.5	44	N/A

* The power is not measured since no electrical load is used in thermal cycling experiment

Chapter 5.   Morphing Materials: Shape Memory Polymers and Shape Memory Alloy Nanofibers

5.1 Objective of Current Research

The goal of this research is to develop a two-way reversible shape-changing composite capable of large deformations. To accomplish this task, a composite material with a shape memory polymer matrix, and shape memory alloy wire reinforcements is proposed. Neither material on its own possesses the properties necessary to achieve this goal, but it may be achieved by combining the properties of these materials.

5.2 Shape memory polymers

Shape memory polymers (SMPs) are a unique type of polymer that through a special thermomechanical cycle can return to its original shape after being fixed in deformed temporary shape. One of the most prominent SMPs is Polyurethane (PU). PU produced for shape memory properties is generally synthesized by reacting a linear long chain diol (either a polyether or polyester) with excess isocyanate to form a prepolymer, followed by the addition of a short chain diol that acts as a chain extender to link the prepolymers together. Due to the thermodynamic imicisibility of segments of PU, phase separation into a flexible soft segment (long chain diol) and a rigid hard segment (isocyanate + chain extender) occurs. Both physical and covalent cross-linking between the hard segments of PU chains can occur. This cross-linking between the hard segments gives PU the ability to exhibit the shape memory effect. Depending on the length of the soft segment chain of PU, the shape memory transition temperature can correspond to either T_g or T_m of the soft segment. In this study the long chain diol used was Poly(tetramethylene glycol) (PTMG, MW 2000), 4,4' Methylenebis(phenylisocyanate) (MDI) was the isocyanate, and the chain extender 1,4 butanediol (BD).

Figure 5.1 shows the differential scanning calorimetry (DSC) measurements made on two samples of PU processed by the same method, but with different molar ratios of the isocyanate functional groups to hydroxyl functional groups (NCO:OH) of the reactants. The black line was a PU with a ratio of 1:1 and the orange line was a PU with a ratio of 5:3. As it can be seen from the figure, the addition of excess NCO groups dramatically changes the structure of the materials, going as far as changing the properties of the PU from a thermoplastic to a thermoset. A literature search revealed that a molar ratio of NCO groups to OH groups greater than 1.1 can result in changes of PU from a thermoplastic to a thermoset due to cross-linking and other reactions of the isocyanate groups with the other functional groups in the chain. [Hepburn, 1992] However, during the initial prepolymer reactions the NCO:OH ratio is always greater than 2 due to use of excess isocyanate to used to cap the ends of the long chain diol. Depending on the composition the ratio can be >8 before the chain extender is later added to bring the ratio back to 1:1.
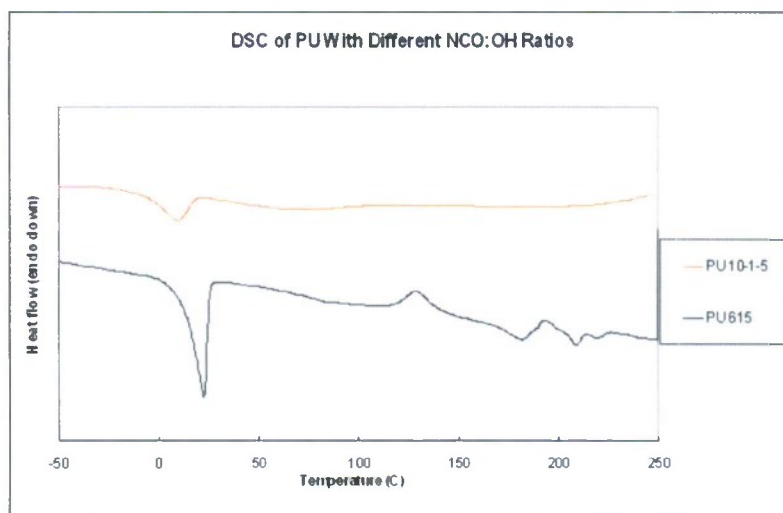
Figure 5.1: DSC measurements of PU with different NCO:OH ratios

Since the shape memory properties of PU are dependent upon the phase separation, three different synthesis methods were used to determine the effect of excess isocyanate groups on the structure of PU. Synthesis method A is the method commonly found in literature (Lee, et. al, 2001). It consists of reacting all of the MDI and PTMG together under a nitrogen atmosphere in N,N dimethylacetamide at 80°C in the first step to form the prepolymer. In the second step BD is added into the solution to extend the polymer chains and form PU. In synthesis method B MDI, PTMG, and BD were all reacted together at 80°C under nitrogen atmosphere in one step. The purpose of this method was to see if a ratio of NCO:OH of 1:1 throughout the entire reaction would effect the amount of phase separation in PU. Synthesis method C was similar to A, except that only half of the MDI was used in the first step and the other half was added with the BD in the second step. In this method, the excess NCO groups available to react during the first step is reduced, however, the remaining NCO is added in the second step when the NCO:OH ratio is closer to 1. The molar ratios for the two compositions studied and the amount used in each step of the reaction can be seen in Table 5.1. In this paper the specimens are designated by its composition and synthesis method (e.g. PU 615A means 6 mol MDI, 1 mol PTMG, 5 mol BD, and made by method A)

Table 5.1: Molar ratio of reactants for PU synthesis methods

Synthesis Method	Step 1: Molar ratio of reactants			Step 2 Molar ratio of reactants		
	MDI	PTMG	BD	MDI	PTMG	BD
PU 615A	6	1	0	0	0	5
PU 615B	6	1	5	-	-	-
PU 615C	3	1	0	3	0	5
PU 817A	8	1	0	0	0	7
PU 817B	8	1	7	-	-	-
PU 817C	4	1	0	4	0	7

For testing, films of each specimen were prepared by casting the reaction solution on a glass substrate and allowing the solvent to evaporate off to form a PU film. After the solvent had evaporated the film was soaked in water for approximately 24 hours to facilitate easy separation

of the film from the substrate. After removal, the film was subsequently dried in a vacuum oven at 100°C for 24 hours to remove excess moisture and solvent.

To determine the transitions temperatures and also to see how the different synthesis methods affected the structure of the PU samples, DSC measurements were made. The temperature range for the DSC measurements was -50-250°C at a heating rate of 5°C/min. All samples measured had a mass between 9.8-10.2 mg and each sample was heated to 250°C and slowly cooled prior to taking the DSC measurement to remove any inhomogeneities in the samples due to processing. In Figure 5.2 below are the DSC results for the PU 615x series. From this plot it can be seen that all 3 samples exhibit peaks near room temperature that corresponds to the melting of the soft segment (the transition temperature for these SMPs). However, only 615B and 615C show significant hard segment crystallization. The lack of hard segment crystallization for 615A means that there may be more phase mixing present in the sample that would hinder the crystallization. From the enthalpy of melting data of the soft segment, ΔH_m, it can be seen that the soft segment of 615C is the most crystalline of the 3 samples. Combined with the presence of the hard segment crystallization peaks, this indicates that 615C has the greatest amount of phase separation.
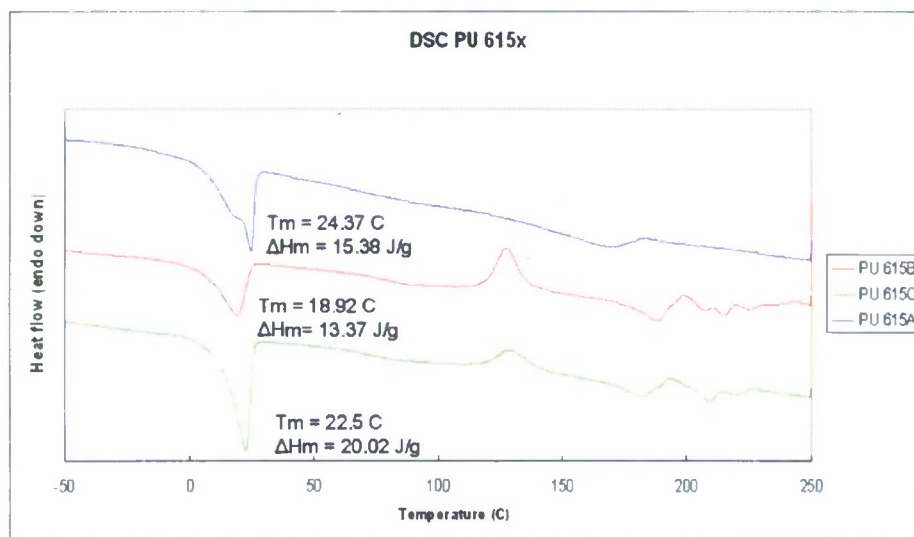

Figure 5.2: DSC chart of PU 615x series

The DSC data for the 817 series can be seen in Figure 5.3. As expected, as the hard segment content increases the size of the soft segment melting peaks decreases and hard segment crystallization peaks become stronger. The trends for the peaks are similar to the DSC charts for the 615x series with the one exception being that ΔH_m for 817B is slightly greater than 817A. T_m for the 817x series were found to be 6°-8°C lower than the samples from the 615x series synthesized by the same method. Although 817A does show hard segment crystallization, the peaks are smaller and broader than those of the other samples, which is indicative of phase mixing.
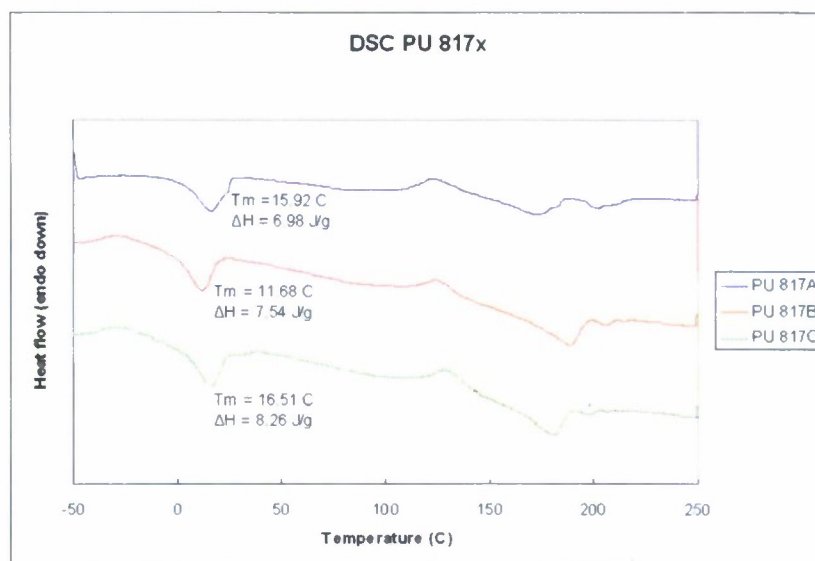
Figure 5.3: DSC chart for PU 817x series

The shape memory cycle was performed using an Instron testing frame. To heat the sample, infrared lamps were mounted on both sides of the Instron frame. Cooling of the sample below room temperature was accomplished by blowing air chilled by passing it through coiled pipes submerged in a dewar filled with liquid nitrogen. The first step of the shape memory cycle was heating the sample to $T_m + 20°C$ at a rate if 5°C/min, while keeping the load at zero. The sample was then extended to 50% strain (ε_{pre}) at a rate of 10 mm/min. After reaching ε_{pre}, the strain was held constant as the temperature was cooled to $T_m - 20°C$, the cooling rate was not constant and fairly rapid (~>20°C/min) due to the limitations of the setup. Once the lower temperature had equilibrated, the load on the sample was set to zero. The resulting strain after stress was equal to zero was called $\varepsilon_{fix.}$. The sample was then heated back up to $T_m + 20°C$, while keeping the zero load condition. The remaining strain was called the residual strain, ε_r. Results of the shape memory for the PU 615x series can be seen in Figure 5.4. Shape memory testing results for the PU 817x series were not obtained due to problems obtaining good quality films and also the need to start focusing on the shape memory alloy nanofibers.
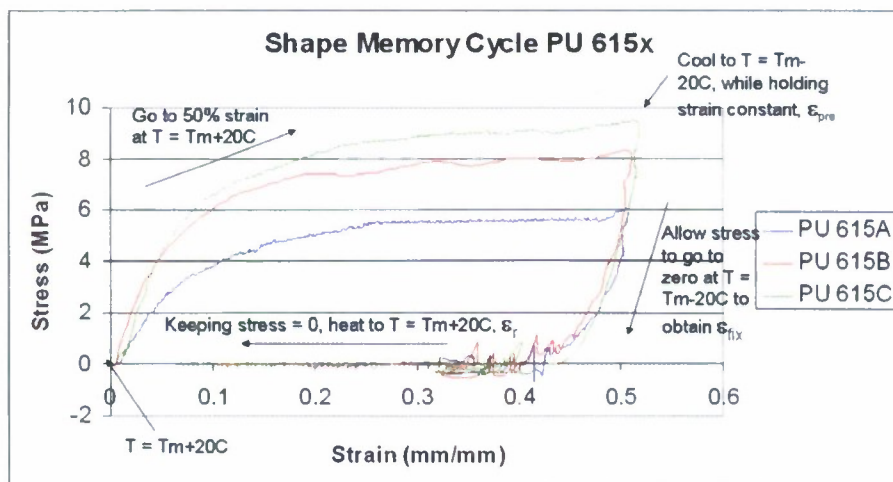

Figure 5.4: Stress vs. Strain for shape memory cycle of PU 615x

As it can be seen from the figure above, PU 615C exhibited the greatest strength during the shape memory cycle. As expected, the samples with the greater hard segment crystallization (615B and C) displayed greater mechanical properties than 615A. The zigzagging back and forth as the load was set to zero was caused by overshoot of the Instron's LVDT as it tried to reach a position where there was zero load on the polymer. The shape memory properties of the PU 615x series can be seen in Table 5.2. The equations used to calculate the amount of shape retention and recovery are given below:

$$\text{Shape Retention} = \frac{\varepsilon_{fix}}{\varepsilon_{pre}} \tag{5.1}$$

$$\text{Shape Recovery} = \frac{\varepsilon_{pre} - \varepsilon_r}{\varepsilon_{pre}} \tag{5.2}$$

Table 5.2 Shape Memory Properties of PU 615x series

Sample	Peak Stress (MPa)	ε_{fix}	ε_r	Shape Retention (%)	Shape Recovery (%)
615A	6.08	.371	.068	74.2	86.4
615B	8.35	.375	.061	75.0	87.8
615C	9.46	.369	.057	73.8	88.6

The shape retention numbers for these samples are somewhat low; this may be to due to the uncontrolled cooling rate, which could have affected the ability of the chains to fully crystallize. However, in general SMPs that transition around T_m will have less shape retention than those around T_g due to the fact that most polymers chain do not fully crystallize. From this data it can also be seen that although there was difference in the mechanical properties of specimen, there was not a significant difference in the shape memory properties. This may also be a result of the cooling rate. Kinetic studies of phase separation in PU have shown that after rapid quenching, it can take up to several days for the sample to regain equilibrium. (Drobny, 2007)

Figure 5.5 below shows a PU specimen being put through a shape memory cycle. In Figure 5.5a the original shape of the specimen can be seen. Figure 5.5b shows the fixed shape of the specimen after it has been heated to 50°C, twisted around a small mandrel and submerged in an ice bath at ~1°C while still being constrained on the mandrel. Figures 5.5c and 5.5d show the sample before and after it was placed in a 50°C water bath and 5.5e is the final recovered shape. The time for the shape recovery to occur was approximately 2-3 seconds.
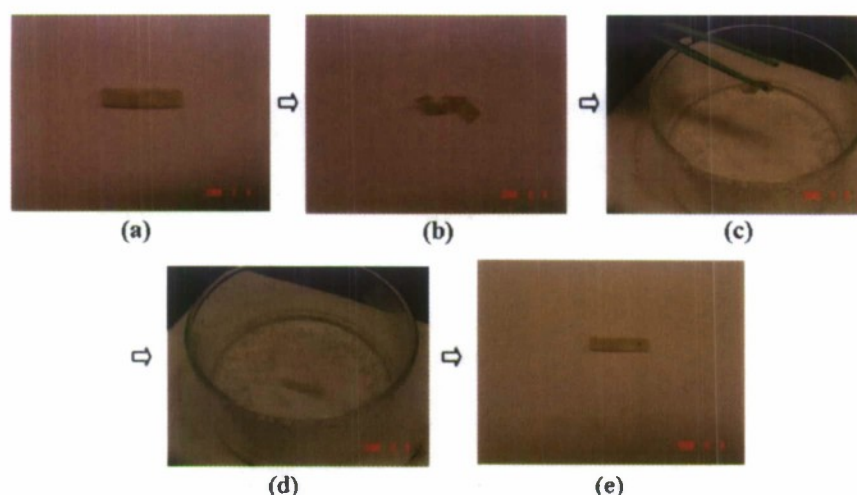
Figure 5.5: Shape memory cycle of PU (a) at RT (b) after shape fixing (c) before being placed in 50°C water bath (d) after placing in water bath (e) recovered shape

5.3. Shape Memory Alloy Nanofibers

Electrospinning is a process that has been used to produce polymer, composite, and ceramic nanofibers. However, use of electrospinning as a means of producing metal nanofibers is not well studied; in fact there is almost no literature available on the subject. Although most electrospinning solutions used for non-polymer fibers use ions dissolved in the solution, achieving the correct stoichiometric ratio of the ions in solution chemistry often requires extensive experimentation. For this reason, it was decided to try using equiatomic NiTi nanoparticles in the polymer solution followed by heat treatment to burn off the polymer and sinter the particles together to create the metal nanofibers.

One limitation of the electrospinning process is that in most cases only it is very difficult to collect individual nanofibers. In a basic electrospinning process with a flat conducting collector, a web of interconnected nanofibers is formed that cannot be separated due to entanglements in the structure. Aligned nanofibers can be produced by using rotating collectors such as a drum; however, collection of individual nanofibers is still difficult. (Ramakrishna et. al, 2005). In order to try and create separated fibers we tried placing insulation around the syringe used for electrospinning. Placing an insulating box that extends a few cm beyond the tip of the needle reduces the deposition area of the fibers, but also produces fibers that form vertically on the collector (Fig 5.6b). The addition of a simple paper mesh (hole size 1cm x 1cm) over the opening of the box (Fig. 5.6a), allows for separation of the fibers formed between the mesh and the target into individual fibers (Fig 5.6c). The mesh prevents the formation of the mat of fibers on the target as well.
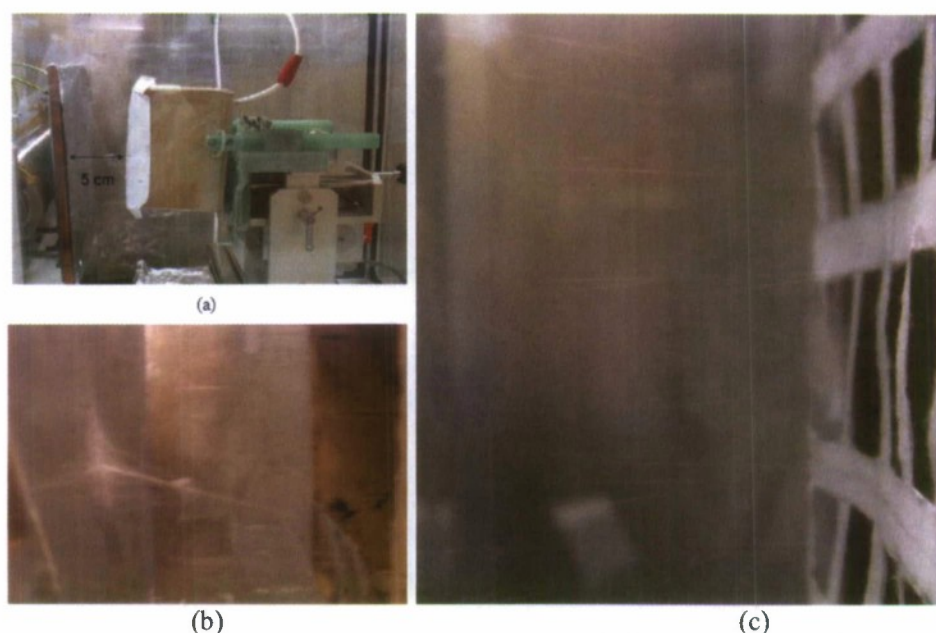
Figure 5.6: (a) Setup of electrospinning with paper mesh (b) mat and fibers formed with insulating box (c) Separate fibers formed with paper mesh

With the paper mesh, the majority of the fibers form in less than 5-10 secs after the voltage is applied, but after that period of time the rate of fiber formation decreases dramatically. This is most likely caused by repulsion due to residual charge on the fibers (only a small portion of the fiber is in contact with the grounded target) and the formation of fiber webs similar to those found in other electrospinning experiments over the holes in the mesh. After a few runs, the mesh needs to have the fibers cleared out and/or be replaced with a new mask in order for fiber production to continue. Fibers can be collected by cutting the fibers near the mask and extracting them from the target.

In this study, the solution used for electrospinning was prepared by first dissolving Poly(vinyl acetate) (PVAc, MW 500,000) in Tetrahydrofuran (THF), followed by mechanical stirring of the nanoparticles into the polymer solution. This solution used for electrospinning will be called solution A. Composition of all the solutions used for electrospinning can be found in Table 5.3 at the end of this section. The electrospinning experiments were performed with voltages ranging for 15-17.5 kV and a distance from the mesh to the collector of 5 cm. The distance between the tip of the syringe and the collector was approximately 10 cm. The first PVAc fibers with embedded NiTi particles had diameters ranging from 2-20 μm. In addition to the large diameter, many fibers did not have uniform diameters along the length and some fibers exhibited large beads. These beads are not uncommon in electrospinning experiments and are generally found when the viscosity is low and surface tension has a dominant influence on the electrospun jet. However, in this case EDAXS analysis showed that the bulges were likely due to agglomeration of NiTi particles in the fiber. The large diameter of the fibers may have been a result of particle agglomeration as well, or could have been a result of the viscosity of the solution and the strength of the electric field applied during the electrospinning process. SEM images of fibers produced from solution A can be seen in Figure 5.7.
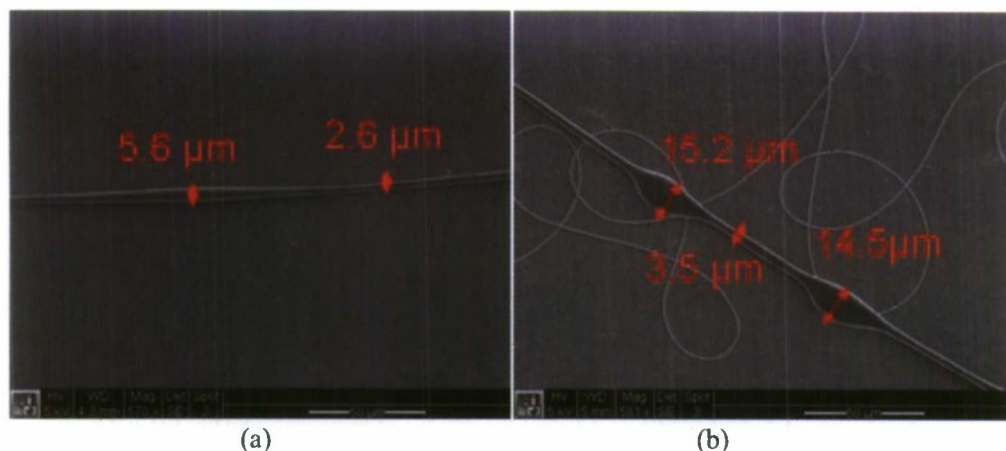
(a)   (b)

Figure 5.7: SEM images of fibers made from solution A (a) Fibers with varying diameter (b) Beads in the fibers.

To prevent agglomeration of the NiTi particles found in the first fibers, a repellant was added to the solution. This solution was prepared by making two separate solutions: a solution of PVAc dissolved in THF and a solution containing the NiTi nanoparticles and the repellant. In the second solution, the repellants, Oleic acid and Oleylamine, were added into THF and then the NiTi nanoparticles were mixed into solution for 30 min. These two solutions were then mixed and stirred together to obtain the electrospinning solution (solution B). Solution B produced fibers of more consistent diameter (1-5 μm), but the fiber diameters were still not submicron as seen in Figure 5.8 below.
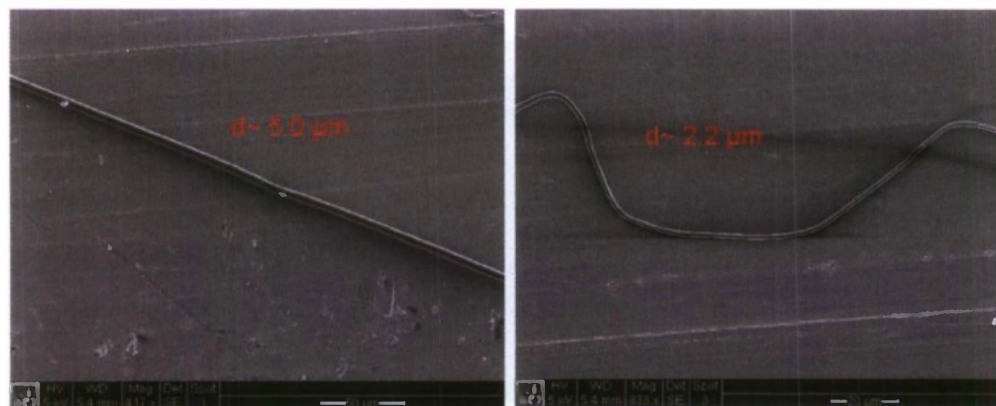

Figure 5.8: SEM images of fibers made from solution B

Varying the electrospinning parameters of voltage and distance to the collector had a small effect on the diameter of the fibers, but it was found to be much smaller than altering the properties of the solution. To determine the best conditions for preparation of the electrospinning solution, the distribution and size of the NiTi particles in the polymer leftover after drying the solution were observed under SEM. Two different samples of both, the electrospinning solution and the solution containing only the repellant and NiTi particles were made. One sample of each solution was subjected to mechanical stirring, while the other sample was subjected to sonication. The repellant solution showed a good distribution of particles for both cases. However, the electrospinning solution displayed much better dispersion of the particles by mechanical stirring. As it can be seen in Figure 5.9a, the ultrasonic mixing of the electrospinning solution resulted in the particles grouping together. Mechanical stirring showed a uniform distribution with only a

small amount of clustering (Fig. 5.9b). It was also found that less clustering occurred when the concentration of the polymer and particles in the solution was reduced.
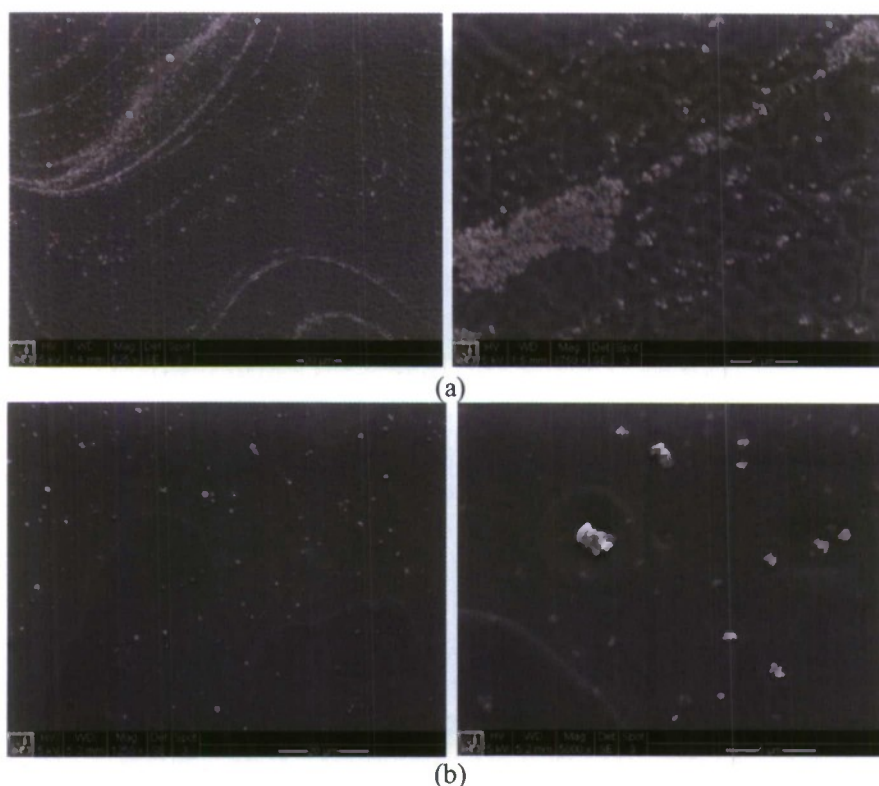

(a)

(b)

Figure 5.9: SEM images of electrospinning solution mixed by (a) sonication (b) mechanical stirring

Using the new solution (solution C), most of the new electrospun fibers had diameters on the range of ~300-600 nm. Beading was still observed in a few fibers, but the frequency and size of the beading had been greatly reduced (beads on the size of 1-1.5 μm). Images of some of these fibers can be seen in Figure5.10.

5.10: SEM images of PVAc fiber with embedded NiTi nanoparticles with submicron diameters

Table 5.3 below contains the compositional information of all the electrospinning solutions detailed above.

Table 5.3: Composition of electrospinning solutions

Solution	Wt % PVAc in solvent	Wt % NiTi Nanoparticles	Mixed with repellant solution	Fiber Diameter (μm)	Notes
A	10.7	1.8	No	2-20	Large beads
B	10.7	1.8	Yes	1-5	constant diameter
C	6.8	1.0	Yes	0.3-0.6	constant diameter

After the electrospinning process, the fibers require further processing to obtain NiTi nanofibers. The first step in the process is calcination the polymer surrounding the fiber. Due to the possibility of carbide formation from the carbon residue of the polymer during processing (Fu, Moochhala, Shearwood, 2004), complete removal of the polymer from the sample is important. Using thermogravitional analysis, the thermal decomposition temperature of PVAc was found to be approximately 550C. To avoid oxidation of the NiTi particles and remove the volatiles from burning off the polymer the fibers are heated under constant vacuum. After removing the polymer matrix, the temperature was increased to sinter the NiTi particles into a nanofiber. Consolidation of the particles into a nanofiber has not yet been achieved, but this work is still in the preliminary stages. Due to the limited amount of literature available for the sintering of NiTi nanoparticles, the sintering time and temperature are still under investigation. So far temperatures of 800, 850, 900°C have been tried resulting in only partial consolidation of the fiber SEM images of the particles after a heat treatment of 850°C for 1 hr can be seen in Figure 11.
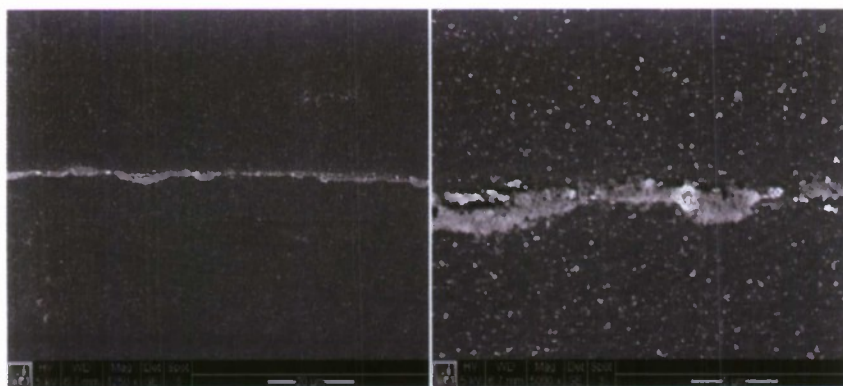

Figure 5.11: SEM images of partially consolidated nanofiber heated at 850°C for 1 hr

The effectiveness of this method for producing NiTi nanofibers with the shape memory effect is still under investigation. Due to the long time at high temperatures that will be mostly likely required for sintering the NiTi particles the shape memory properties of the material could be affected, thus production of NiTi fibers from solution will also be investigated. This work has shown that this electrospinning method can be used to create nanofibers with embedded particles that may be useful for other applications. Once SMA nanofibers are successfully made they will be incorporated into a SMP in an attempt to achieve a two-way reversible shape changing composite.

Chapter 6.   Conclusion

We have developed the design and processing route of three different kinds of active composites, (1) ferromagnetic shape memory alloy composite, (2) SMA-piezo composite and (3)

SMA fiber /shape memory polymer(SMP) composite. As to the third one, we are still progressing toward the optimization of the SMA nanofiber processing and SMA fiber/SMP composite as this was started most recently. The main conclusive remarks are given in the following.

1. Ferromagnetic SMA composite was successfully designed and processed as a fast-responsive airborne actuator material which is very cost effective. Use of spark plasma sintering was effectively demonstrated in processing ferromagnetic SMA composite. The properties of the as-processed ferromagnetic SMA are compared with the predictions by the Eshelby modeling, resulting in good agreement.

2. Design of a new SMA-piezo composite was proposed as multi-functional material, for fast-responsive actuator material and thermal energy harvester where the synergistic effects of coupling SMA and piezoelectric phases are demonstrated.

3. Attempt of processing SMA nanofibers via electrospinning was made although the post annealing still remains to be optimized so as to make continuous solid SMA fibers.

4. Several shape memory polymers are designed, and processed, which exhibits one-way type shape memory behavior. In this project, we focused mainly polyurethane based SMP as model SMP material. It is expected that combination of the above SMA nanofibers and SMP would result in both-way type shape memory property which is considered new type of morphing material which can exhibit larger shape change which is reversible upon temperature change. It is recommended that use of higher stiffness SMP is to be used as SMP, such as epoxy and polyimide for aerospace applications as these would exhibit higher stiffness and match as a partner constituent material with SMA fibers.

References

Allafi J. K., Dlouhy A. and Eggeler G. (2003) Influence of precipitation and dislocation substructure on phase transformation temperatures in a Ni-rich NiTi-shape memory alloy. Journal Physique. IV Proceedings, 2003; 212:681-684.

Arsenault, R.J., Taya, M. , (1987). Acta Metall. 35, 651.

Badcoek, R. A., Birt, E. A. (2000). The Use of 0-3 Piezocomposite Embedded Lamb Wave Sensors for Detection of Damage in Advanced Fiber Composites. Smart Material and Structures, 9: 291-297.

Banno, H. (1983). Recent Developments of Piezoeleetric Ceramic Products and Composites of Synthetic Rubber and Piezoelectrie Ceramie Partieles. Ferroeleetries, 50: 3-12.

Beleggia M. and De Graef. M. (2003) Journal of Magnetism and Magnetie Materials. Vol. 263, L1-9.

Birman, V., "Review of Meehanies of Shape Memory Alloy Structures," Applied Mcehanies Reviews, vol 50(11), pp. 629-645, 1997.

Boyd, J. G., Lagoudas, D. C., "A Thermodynamical Constitutive Model for Shape Memory Materials - Part I: The Monolithie Shape Memory Alloy", Int. J. of Plastieity, vol 12, pp. 805-842, 1996.

Brinson, L. C., "One Dimensional Constitutive Behavior of Shape Memory Alloys: Thermomechanical Derivation with Non-Constant Material Functions," J. of Intell. Matl. Syst. and Struet., vol. 4:2, pp. 229-242, 1993.

Chen, T. Y. (1994). Some Exaet Relations of Inelusions in Piezoelectric Media. International Journal of Engineering Science, 32: 553-556.

Chikazumi S. (1964) Physies of Magnetism, New York, Wilcy.

Deeg, W. F., (1980). The Analysis of Disloeation, Craek and Inelusion Problem in Piezoelectric Solids. PhD Dissertation, Stanford University.

Drobny, J.G., Handbook of Thermoplastie Elastomers, William Andrew Publishing, 2007, pp.215-230.

Dunn , M.L., Taya, M. , (1993b). Proe. Roy. Soe. London. A443, 265.

Dunn, D. L., Taya, M. (1993). Mieromeehanies Predietions of the Effeetive Electroclastic Moduli of Piezoelectric Composites. International Journal of Solids and Structures, 30: 161-175.

Dunn, M. D. (1993a). Exact Relations Between the Thermoelectroelastic Moduli of Heterogeneous Materials. Proeeedings of the Royal Society of London A, 441: 549-557.

Dunn, M. D. (1993b). Mieromeehanies of Coupled Eleetroelastie Composites: Effective Thermal Expansion and Pyroelectric Coeffieients. Journal of Applied Physics, 73(10): 5131-5140.

Dunn, M. L. (1994). Thermally Induced Fields in Eleetroelastic Composite Materials: Average Fields and Effeetive Behavior. Journal of Engineering Materials and Tcehnology, 116: 200-207.

Dunn, M. L., Taya, M. (1993). An Analysis of Composite Materials Containing Ellipsoidal Piczoeleetrie Inhomogeneities. Proeeedings of the Royal Soeiety of London, Series A, 443: 265- 287.

Dunn, M.L., Taya, M. , (1993a). Intl. J. Solids. Struct. 30, 161.

Engel, T. G. "Energy conversion and high power pulse production using miniature piezoelectric compressors," IEEE Trans. Plasma Sci., vol. 28, no. 5, pp. 1338-1340, Oct. 2000.

Eshelby, J. D., "The Determination of the Elastic Field of an Ellipsoidal Inclusion, and Related Problems," Proc. Roy. Soc. London vol. 241 , pp. 376-396, 1957.

Fu, Y., Moochhala, S., and Shearwood, C, Proc. of the SPI, v. 5275, n. 1 (2004), pp.9-17.

Gabbert, U., Kreher, W., Ko¨ppe, H. (1999). Mathematical Modeling and Numerical Simulation of Smart Structures Controlled by Piezoelectric Wafers and Fibers. In: Proceedings of the EUROMAT '99 Conference, Munich.

Glynne-Jones, P., Beeby, S. P., White, N. M., "Towards a piezoelectric vibration-powered microgenerator," IEE Proc. Sci. Meas. Technol., vol. 148, no. 2, pp. 68-72, 2001.

Gururaja S., Nakayama H. and Taya M. (2006) Processing of ferro-magnetic shape memory alloy (Fe-NiTi) composite using spark plasma sintering. Proceedings of the SPIE – The international Society for Optical Engineering, Vol. 6170, pp. 617018.

Gururaja S., Taya M., Nakayama H., Kang Y.S., A. Kawasaki and Y.Sutou (2005) Effective magnetic properties of Fe-NiTi (FSMA) particulate composite. Proceedings of the SPIE – The international Society for Optical Engineering, Vol. 4761, pp. 548 – 556.

Hagood N.W. et al., "Development of micro-hydraulic transducer technology," in Proc. 10th Int. Conf. Adaptive Structures and Technologies, Paris, France, Oct. 1999, pp. 71-81.

Harrison, W.B. (1976). Flexible Piezoelectric Organic Composites. In: Smith, P.L. and Pohanka (eds.), Proceedings of the Workshop on Sonar Transducer Materials. National Research Lab, Washington, D.C., 257-268.

Hatta, H., Taya, M. , (1986). J. Appl. Phys. 59, 1851.

Hatta, H., Taya, M. , (1986). Intl. J. Eng. Sci. 24, 1159.

Hepburn, C., Polyurethane Elastomers 2nd Edition, Elsevier Applied Science, 1992.

Hugo Schmidt, V. "Piezoelectric energy conversion in windmills," in Proc. Ultrasonics Symp., 1992, pp. 897-904.

Hwang, J. H., Yu, J. S. (1994). Electroelastic Eshelby Tensors for an Ellipsoidal Piezoelectric Inclusion. Composites Engineering, 4(11): 1169-1182.

Ikeda, T., 1990, Fundamentals of Piezoelectricity, Oxford, Oxford University Press

James R.D., Wuttig, M. (1998) Magnetostriction of martensite. Philosophical Magazine A: Physics of Condensed Matter: Structure, Defects and Mechanical Properties, Vol. 77, pp. 1273 – 1299.

James, R. D. Tickle, R., Wuttig, M. (1999). Materials Science and Engineering A, 273 ,320.

Jiang , B., Batra, R.C. (2002). Continuum Mech. Thermodyn. 14, 87.

Jiang, B., Fang, D. N., Hwang, K. C. (1999). A Unified Model for the Multiphase Piezocomposites with Ellipsoidal Inclusions. International Journal of Solids and Structures, 36(18): 2707-2733.

Kakeshita T., Takeuchi T., Fukuda T., Tsujiguchi M., Saburi T., Oshima R. (2000) Giant magnetostriction in an ordered Fe3Pt single crystal exhibiting a martensitic transformation. Applied Physics Letters, Vol. 77, pp. 1502 – 1504.

Kato H., Wada T., Liang Y., Tagawa T., Taya M., Mori T. (2002) Martensite structure in polycrystalline Fe-Pd. Materials Science Engineering A, Vol. 332, pp. 134 – 139.

Kato, H. , Wada, T. , Tagawa, T. , Liang , Y., Taya, M. (2001). Proc. of 50th Anni. of Japan Society of Mater. Sci., Osaka, May 21-26, 296.

Kuo , W.S., Huang, J.H. (1997). Intl. J. Solids. Struct. 34, 2445.

Kusaka M. and Taya M. (2004) Design of Ferromagnetic Shape Memory Alloy Composites. Journal of Composite Materials, Vol. 38, No. 12, pp. 1011-1035.

Kymissis, J, Kendall, C., Paradiso, J.J., Gershenfeld, N., "Parasitic power harvesting in shoes," in Proc. 2nd IEEE Int. Conf.Wearable Computing, Los Alamitos, CA, Aug. 1998, pp. 132-139.

Lee, B.S, Chun, B.C, Chung, Y, Sul, K.I., and Cho, J.W., Macromolecules, v.34 (2001), pp. 6431-6437.

Li, J. Y., Dunn, M. L., 1998 Phil. Mag., A77 (5), 1341-1350

Li, J. Y., Dunn, M. L., Ledbetter, H. M., 1999, J. Appl. Phys., 86(8), 4626-4634

Li, J.F. , Takagi, K. , Terakubo, N., Watanabe, R. (2001). App. Phys. Lett. 79, 2441.

Liang Y., Kato H., Taya M., Mori T. (2001) Straining of NiMnGa by stress and magnetic fields. Scripta Materiala, Vol. 45, pp. 569 – 574.

Liang Y., Taya M. (2006) Model calculation of 3D-phase transformation diagram of ferromagnetic shape memory alloys. Mechanics of Materials, Vol. 38, pp. 564-570.

Liang Y., Wada T., Kato H., Tagawa T., Taya M., Mori T. (2002) Straining of a polycrystal of Fe-Pd with martensite structure by uniaxial loading. Materials Science Engineering A, Vol. 338, pp. 89-96.

Liang, Y., Kato H., Taya, M. (2000). Proc. Plasticity '00: 8th Int. Symp. on Plasticity and Current Applications, 193.

Liang, C., Rogers, C. A., "One-Dimensional Thermomechanical Constitutive Relations for Shape Memory Materials," J. of Intell. Matl. Syst. and Struct., vol. 1, pp. 207-235, 1990,

Mamedov V. (2002) Spark plasma sintering as advanced PM sintering method. Powder Metallurgy, Vol. 45, No. 4, pp. 322-328.

Mikata, Y. (2001). Intl. J. Solids. Struct. 38, 7045.

Mikata, Y., "Determination of piezoelectric Eshelby tensor in transversely isotropic piezoelectric solids," Int. J. of Engineering Science, vol.38, pp. 605-41, 2000.

Miyazaki S., Otsuka K., 1984 Mechanical behavior associated with the premartensitic rhombohedral-phase transition in a Ti50Ni47Fe3 alloy Phil. Mag. A 50 393-408

Miyazaki S., Otsuka K0,. 1986 Deformation and transition behavior associated with the R-phase in Ti-Ni alloys Metall. Trans. A 17 53-63

Mori, T., Tanaka, K. (1973). Average stress in matrix and average elastic energy of materials with misfitting inclusion. Acta Metallurgica, 21: 571-574.

Murray, S. J. , Frinelli, M. , Kantner, C. , Huang, J. K. , Allen, S. M., O'Handley, R. C. (1998). Journal of Applied Physics, 83 (1998) 7297.

Newnham, R. E., Bowen, L. J., Klicker, K. A., Cross, L. E. (1980).Composite Piezoelectric Transducers. Materials in Engineering, 2: 93-106.

Newnham, R. E., Skinner, D. P., Cross, L. E. (1978). Connectivity and Piezoelectric-Pyroelectric Composites. Materials in Engineering, 2: 93-106.

Odegard, G.M. (2004). Aeta Mater. 52, 5315.

Osborn J.A. (1945) Physical Review. Vol. 67, No. 11 and 12:351-357

Otsuka K., (1990). Introduction to the R-phase transformation Engineering Aspects of Shape Memory Alloys ed T W Duerig et al (London: Butterworth-Heinemann) pp 36-45

Otsuka, K., Wayman, C. M., Shape Memory Materials, Cambridge University Press, Cambridge, UK, (1998).

Qin, Q.H., (2004)., Comp. Struct. 66, 295.

Ramakrishna, S. et.al, An Introduction to Electrospinning and Nanofibers, World Scientific, 2005. pp. 135-140.

Roundy, S., "The power of good vibrations," Lab Notes-Research from the College of Engineering, University of California, Berkeley, vol. 2, no. 1, Jan. 2002.

Shenck, N. S., Paradiso, J., "Energy scavenging with shoe-mounted piezoelectrics," IEEE Micro, vol. 21, no. 3, pp. 30-42, May-Jun. 2001.

Smith, W. A., Auld, B. A. (1991). Modeling 1-3 Composite Piezoelectrics: Thickness-Mode Oscillations, IEEE Transactions on Ultrasonics, Ferroelectrics, and Frequency Control, 38: 40-47.

Sohmura, T., Oshima, R., Fujita, F.E. (1980). Seripta Metallurgiea, 14 ,855-856.

SPS Syntex Inc. manual. http://www.scm-sps.com/ Last Accessed: 02/20/07.

Takagi, K. , Li, J.F. , Yokoyama, S. , Watanabe, R. , Almajid, A., Taya, M. (2002). Sci. & Tech. Adv. Mater. 4, 55.

Tanaka, K., "Thermomechanical Sketch of Shape Memory Effect: One-Dimensional Tensile Behavior," Res Mechanica, vol.18, pp.251-263, 1986.

Tanaka, K., Nagaki, S., "A Thermomechanical Description of Materials with Internal Variables in the Process of Phase Transformation," Ingenieur-Archiv, vol. 51, pp. 287-299, 1982.

Taya, M. (2005). Electronic Composites, 1st ed. Cambridge University Press, Cambridge.

Taya, M., Furuya, Y., Yamada, Y., Watanabe, R., Shibata, S., Mori, T., "Strengthening mechanisms of TiNi shape memory fiber/Al matrix composite" Proc. SPIE 1916, pp. 373-383, 1993

Taya, M., Hayashi, S., Kobayashi, A.S., Yoon, H.S., (1990). J. Amer. Ceram. Soc. 73, 1382

Taylor, G. W., Burns, J. R., Kammann, S. M., Powers, W. B., Welsh, T. R., "The energy harvesting eel: A small subsurface ocean/river power generator," IEEE J. Ocean. Eng., vol. 26, no. 4, pp. 539-547, Oct. 2001.

Ullakko K., Hung J.K., Kokorin V.V., O'Handley R.C. (1997) Magnetically controlled shape memory effect in Ni2MnGa intermetallics. Scripta Meteriala Vol. 36, pp. 1133 – 1138.

Wada T., Liang Y., Kato H., Tagawa T., Taya M., Mori T. (2003) Structural change and straining in Fe-Pd polycrystals by magnetic field. Materials Science Engineering A, Vol. 361, pp. 75-82.

Wang, B. (1992). Three-dimensional Analysis of an Ellipsoidal Inclusion in a Piezoelectric Material. International Journal Solids and Structures, 29: 293-308.

Zhao Y., Taya M., Kang Y. and Kawasaki A. (2005) Compression behavior of porous NiTi shape memory alloy. Acta Materialia, Vol. 53, No. 2, pp. 337-343